

Improving sound absorption through the filament stringing effect in 3D printed acoustic materials

Tomasz G. Zieliński^{a, ID, *}, Marco D'Agostini^{b, ID}, Andrew Gleadall^{c, ID}, Rodolfo Venegas^{d, ID}, Paolo Colombo^{b, e, ID}, Giorgia Franchin^{b, ID}

^a Institute of Fundamental Technological Research, Polish Academy of Sciences, ul. Pawińskiego 5B, 02-106 Warsaw, Poland

^b Department of Industrial Engineering, University of Padova, Padova 35131, Italy

^c Wolfson School of Mechanical, Electrical and Manufacturing Engineering, Loughborough University, Loughborough, Leicestershire LE11 3TU, UK

^d University Austral of Chile, Institute of Acoustics, P.O. Box 567, Valdivia, Chile

^e Department of Materials Science and Engineering, The Pennsylvania State University, State College, PA 16801, USA

ARTICLE INFO

Keywords:

Prototyping acoustic composites
Exploiting 3D printing imperfections
Fully controlled G-code
Filament stringing
Fibrous fillers
Sound absorption

ABSTRACT

This work demonstrates how a well-known malfunction that frequently occurs in material extrusion technologies, known as filament stringing or oozing, can be used to increase the acoustic performance of 3D printed sound absorbing materials. The purpose is first achieved with conventional slicer software by deliberately setting some printing parameters 'wrong' to provoke filament stringing. Acoustic materials based on the same original design of narrow slits are 3D printed with retraction enabled or disabled, or using a higher than required printing temperature. The uncontrolled filament stringing that occurs in this way creates fibres in the slits, which ultimately affects the sound absorption measured for these materials. This cannot be ignored in modelling if accurate sound absorption predictions are to be obtained. However, inspired by the uncontrolled stringing, we developed a new concept to print parts with deliberate parametrically adjustable micro-fibre substructures. These are achieved by directly designing innovative toolpaths with recently developed design software (*FullControl GCODE Designer*), which has never been used previously for sound absorption purposes. The method permits low-cost 3D printers to produce tailored complex acoustic materials with enhanced viscous dissipation effects and improved sound absorption properties. This behaviour is correctly captured by the proposed, experimentally verified, mathematical model of such acoustic composites. The examples presented in the article are also used to discuss some aspects of the reproducibility of acoustic materials 3D printed by extrusion.

1. Introduction

3D printing of innovative designs of acoustic materials and metamaterials has enjoyed great interest in recent years; examples include non-periodic acoustic metamaterials with spinoid topologies [1], grid-like honeycomb structures [2] and various lattice structures for sound absorption [3], anisotropic metaporous surfaces for broadband absorption [4], sub-wavelength asymmetric absorbers [5], absorbers with coiled-up resonators [6,7], extremely tortuous low-frequency sound absorbers with single or double porosity [8], etc. This is despite numerous problems and constraints related mainly to the available printing resolutions [9] and the impact of 3D printing quality on the acoustic properties of the designed materials manufactured in that way [10–13]. One usually wants to obtain high-quality prints that perfectly reproduce the

idealised geometry with smooth surfaces and accurate 'mathematical' shapes because such geometries are used in the modelling and optimization process. Since this is challenging, it is common practice to update the mathematical model to reflect the actual, i.e. manufactured geometry, or to modify the design used for 3D printing by accounting for the expected deviations [14]. This, of course, and especially the latter case, requires experience in using a specific 3D printing technology in acoustic treatment applications.

Another issue is the imperfections of additive manufacturing, which are often typical of specific technologies [9]. It is well known that the impact of 3D printing imperfections is significant in acoustic materials but can often be beneficial, e.g. surface roughness tends to increase sound absorption [11,12]. Therefore, it makes sense to exploit these imperfections. This, however, requires additional efforts to correctly recognise

* Corresponding author.

E-mail address: tzielins@ippt.pan.pl (T.G. Zieliński).

this impact in relation to the occurring physical phenomena and their modelling. Some of the latest research goes in this direction [14,15]. For example, microporosity, which is often a problem in powder bed technologies, can be useful for acoustic materials, provided the micropores are open and of the right size [14]. Then, the designed and 3D printed pore network of such a double-porosity acoustic material can be appropriately contrasted in size and permeability with the micropores so that pressure diffusion occurs, which is an additional and effective mechanism for dissipating the energy of acoustic waves [16–18,14]. Specific features and imperfections of filament based technologies have also been used to produce acoustic materials with less contrasted double porosity [19]. Many of the imperfections of 3D printing are usually ignored in acoustic modelling, although recently new models and methods have been proposed to take their impact into account. For example, Ciochon et al. [15] proposed a method to take into account the effect of surface roughness by increasing air viscosity in a thin layer – called ‘fluid shell’ – close to the material surface. Usually, the actual 3D printed surface is rough and its roughness can be controlled to some extent by the thickness of the printed layer. The artificial increase in local air viscosity that simulates the increase in the viscous dissipation effects due to roughness (on a surface that is smooth in the simplified geometric model) can be systematically related to the layer height used in 3D printing [12,15].

Recently, specific technological tweaks are being used on modified extrusion 3D printers [20,21] or even unmodified ones to print fabrics and fibrous materials, e.g.: fibrous sound-absorbing materials [22] or 3D spacer fabrics consisting of two layers of fabric and a filler yarn [23]. Johnston and Sharma [22] proposed two methods for 3D printing fibrous sound absorbers: (i) the fibre bridging method in which the filament is extruded between two points with no underlying supports, and (ii) the extrude-and-pull method where a filament droplet is extruded and then the extruder is rapidly pulled away to generate thin fibres. This approach can be used to produce fibro-porous materials [24,25]. All this can be done using *unmodified* low-cost 3D printers.

In this paper, we use filament stringing to increase the acoustic performance of 3D printed sound absorbing materials by adding fibres inside their pore networks. We show that this can be done with conventional slicers by deliberately setting some printing parameters ‘wrong’ to provoke filament stringing, or by using *FullControl GCODE Designer* [26], which allows for full control over the entire fibre creation process and provides better results. In this way, a budget extrusion 3D printer can be used to prototype acoustic materials with designed slits or pore networks filled with tailored fibrous fillers that enhance viscous dissipation effects and thus can significantly improve sound absorption. To verify this postulate, we have developed a model of such acoustic composites.

The outline of the paper is as follows. Samples with original slit patterns, 3D printed with or without fibres in the slits, are presented in Section 2 along with details about the manufacturing process and a thorough examination of slits with fibres created by provoking stringing (oozing) or using *FullControl GCODE Designer* [26]. The acoustic behaviour model for such slotted materials is discussed in Section 3, first for slits without fibres. Then, in Section 3.5, a modification of this model is proposed to take into account the presence of fibres in the slits. Section 4 shows that sound absorption measured for 3D printed samples can be significantly enhanced if fibres are present in the slits, and that the modified model suitable for acoustic composites with fibrous fillers is essential for correct predictions. The conclusions are summarised in Section 5.

With this publication we would like to celebrate 50 years of Professor Keith Attenborough’s work in the field of acoustics. His achievements in research on the propagation and absorption of sound waves in porous materials have been influencing scientists in this field for many years and will undoubtedly continue to do so.

2. Methods for 3D printing slotted materials with (or without) fibres in the slits

2.1. Fractal-based design and manufacturing of a slotted material

Frequent, and often very serious, defects in fused filament fabrication (FFF) [27,9], i.e. the technology used in this study, are those resulting from printing discontinuities. One of the most common is filament stringing. Although special techniques can reduce or even eliminate these defects, the best solution is avoiding discontinuous extrusion in the first place. This is achieved by removing or at least reducing travel moves, i.e. the movement of the print head when it is not extruding filament, although it may uncontrollably leak from the nozzle. Completely removing extrusion discontinuities eliminates leaks and therefore the filament stringing problem. Rather than designing continuous toolpaths from scratch, it may be advantageous to exploit the geometrical properties of certain mathematical entities. Planar space-filling curves allow mapping of a 2D geometry (a surface) onto a continuous 1D geometry (a curve), or in other words, they are able to pass through every point on a surface along a continuous and non-intersecting path, making them ideal toolpaths for continuous extrusion. For this work, the Peano-Gosper curve (PGC) [28,29], a space-filling fractal curve constructed along a triangular grid of points, was selected as the base toolpath design. The PGC is displayed in Fig. 1 (a), though it should be noted that the visualisation only represents an arbitrary section of the curve because, like most space-filling curves, the PGC can seamlessly tile an infinite plane. Considering the use of the PGC as a continuous toolpath, the resulting print would consist of a highly meandering wall forming a uniform pattern of slits where the slit width is kept approximately constant. In this way, a relatively small part of such a pattern (based on an essentially fractal curve) can be representative for the entire geometry, in terms of significant characteristics related to the considered physical phenomena, e.g. sound wave propagation in materials with such a structure. Therefore, it is suitable for homogenisation modelling techniques.

Fig. 1 (b) shows that the PGC is composed of hexagonal unit cells, each containing a single wall segment with length λ and wall thickness d . It should be noted that if the PGC is directly used as an extrusion toolpath, then the wall thickness is equal to the nozzle size, or more generally to the extrusion width. With a constant wall thickness, the geometric porosity ϵ can be tuned by simply modifying the segment length λ via a coherent scaling of the entire curve. Finally, the scaled curve can be trimmed with a desired shape, and the resulting sub-curves joined to obtain the final toolpath as shown in Fig. 1 (c) for the circular shape required in this study.

Fibre-free samples were produced by directly selecting the PGC as extrusion toolpath, ensuring complete extrusion continuity. To this end, a parametric algorithm was implemented in *Rhinoceros3D/Grasshopper3D (R/G3D)* visual programming interface. The algorithm first performs the three steps depicted in Fig. 1, namely: (a) a sufficiently extended section of the PGC is first generated; (b) it is scaled (by modifying λ) to the desired geometric porosity ϵ , taking into account the nozzle size, i.e. the wall thickness d ; (c) the scaled design is trimmed with a circular shape of desired dimensions. When this procedure is accomplished, ninety 0.45 mm-thick layers of the circular fractal-based pattern are stacked to produce a cylindrical design of slotted sample with 29 mm diameter and 40.5 mm height. Such samples are suitable for testing in impedance tubes with an internal diameter of 29 mm, see Fig. 2 (g). In fact, two computer-aided design (CAD) models were generated based on the same PGC pattern: (i) a ‘straight’ CAD model shown in Fig. 2 (a), and (ii) a ‘twisted’ CAD model produced by applying a 1.15° rotation to each of ninety layers, see Fig. 2 (b). By ‘twisting’ the structure, the tortuosity of the slotted material is increased, which ultimately improves its sound absorption capacity, as demonstrated further. In this case, the cumulative twisting angle Ω is equal to 103° across the total height of the cylinder. This value still ensures good inter-layer support. G-code files were generated directly in *R/G3D* from the spatial coordinates of the

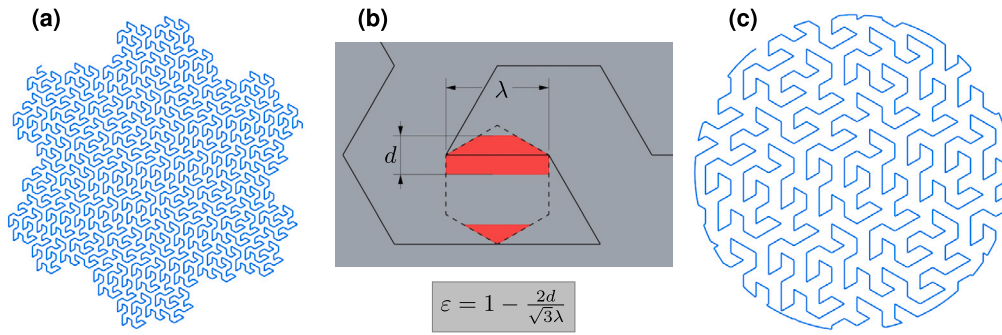


Fig. 1. (a) An arbitrary section of the infinite space-filling Peano-Gosper curve (PGC). (b) Hexagonal unit cell of the PGC with calculation of geometrical porosity ϵ from the wall thickness d and segment length λ . (c) Continuous toolpath based on the PGC trimmed to fit a circular section.

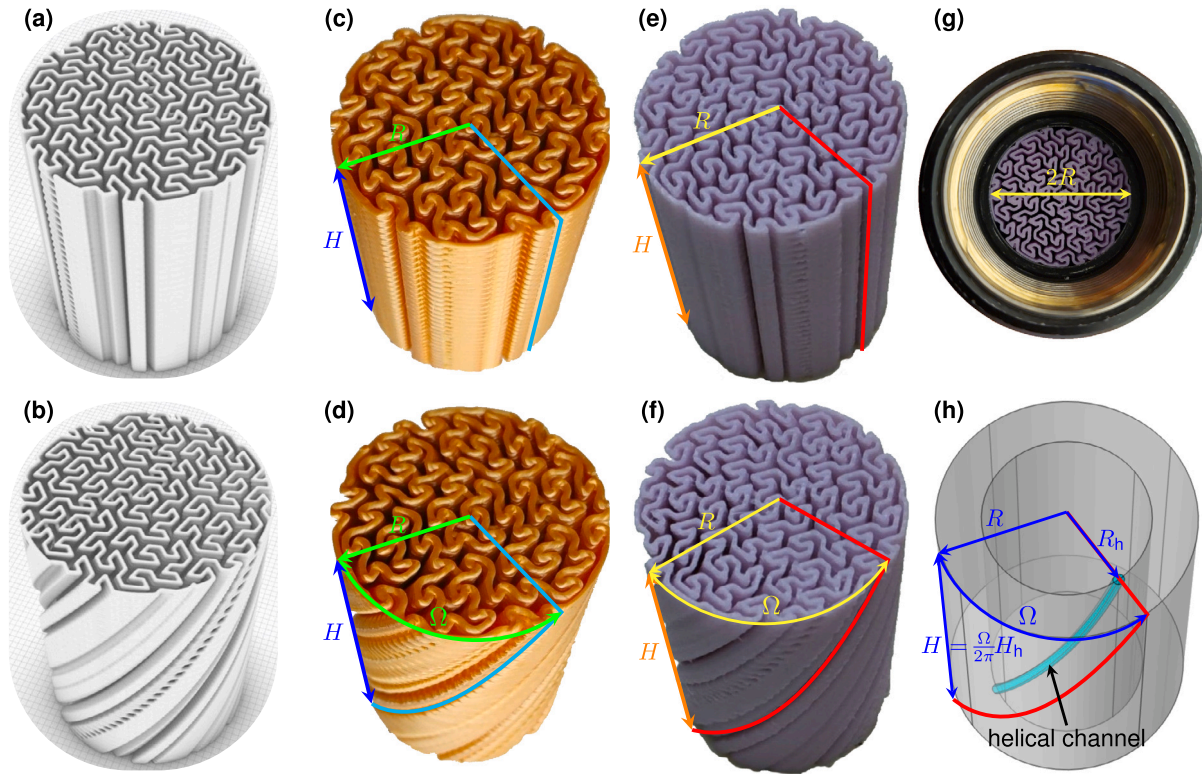


Fig. 2. (a, b) CAD models for: (a) “straight” and (b) “twisted” cylindrical samples. (c, d) PGC-based samples printed from yellow PLA using a 0.6 mm nozzle: (c) a “straight” slotted sample, and (d) a sample with a “twisted” pattern of slits. (e, f) PGC-based samples printed from purple ABS using a 0.4 mm nozzle: (e) a “straight” slotted sample, and (f) a sample with a “twisted” pattern of slits. (g) 3D printed sample inside a 29 mm impedance tube. (h) Helical channel (marked in light blue) with tortuosity equivalent to the twisted slits.

PGC toolpath vertices. It should be noted that the extrusion toolpath described by the PGC presents several sharp corners, so each layer requires a strong support from the layer below in order to obtain a good-quality print. Thus, only a small rotation can be implemented to ensure full support of each layer at all points. Fibre-free samples, see Fig. 2 (c, d), were manufactured on a *Creativity Ender-3* with a 0.6 mm nozzle, using a yellow polylactic acid (PLA) filament to print each of them in ninety 0.45 mm layers. Other printing parameters are listed in Table 1.

2.2. Samples with fibres formed in the slits due to uncontrolled filament stringing

Samples with intentional but uncontrolled stringing were produced by discontinuous extrusion through a conventional slicing approach. The same CAD models for “straight” and “twisted” samples were also used in this case, but the STL files were sliced using a standard slicer software (just as a typical user would do), knowing that this would

cause discontinuities in the print path, leading to uncontrolled filament leakage and stringing. For this purpose, the commercial software *FlashPrint 5* and *UltiMaker Cura* was used with a lower nozzle size (i.e. extrusion width of 0.4 mm) and layer height (0.15 mm). Since in this case the desired wall thickness (0.6 mm) is larger than the extrusion width, multiple passes are required to print each wall segment. As a result, extrusion continuity is lost and frequent travel moves are introduced by the slicers. These new G-codes were printed on a *FlashForge Creator Pro* using three acrylonitrile-butadiene-styrene (ABS) filaments. The ABS filaments have different colours (purple, blue, and red) and come from different manufacturers. These and other important printing parameters are summarised in Table 1 along with information about stringing. Among these parameters are those used for retraction, which in two cases made it even possible to obtain samples containing virtually no fibres, see Fig. 2 (e, f). Therefore, we also 3D printed samples with retraction disabled, which means the retraction distance was set to zero (instead of 1.3 mm, see Table 1). In this way, and also by chang-

Table 1
3D printers and materials used, G-code generation (slicers), printing parameters, and filament stringing.

3D printer:	<i>FlashForge Creator PRO</i>				<i>Creativity Ender-3</i>	
Nozzle size:	0.4 mm				0.6 mm	
G-code generation:	<i>UltiMaker Cura (UMC)</i>	<i>FlashPrint 5 (FP5)</i>		<i>Rhinoceros 3D / Grasshopper 3D (R/G3D)</i>	<i>FullControl GCODE Designer</i>	
Layer height:	0.15 mm				0.45 mm	
Material (filament):	Purple ABS	Purple ABS	Blue ABS	Red ABS	Yellow PLA	Yellow PLA
Print temperature:	230 °C	230 °C	240 °C	240 °C	200 °C	200 °C
Plate temperature:	70 °C	70 °C	70 °C	70 °C	45 °C	45 °C
Printing path:	discontinuous				continuous	
Printing speed:	60 mm/s	60 mm/s	60 mm/s	60 mm/s	15 mm/s	15 mm/s 100 mm/s (for strings)
Retraction distance:	0 or 1.3 mm ^(*)	0 or 1.3 mm ^(*)	1.3 mm	1.3 mm	N.A.	N.A.
Retraction speed:	30 mm/s ^(*)	30 mm/s ^(*)	30 mm/s	30 mm/s	N.A.	N.A.
Stringing:	uncontrolled low or none ^(*)	uncontrolled high or low ^(*)	uncontrolled low/moderate	uncontrolled high	none	controlled 30 or 60 s.p.l.

^(*) when retraction is on; N.A. = not applicable; s.p.l. = strings per layer.

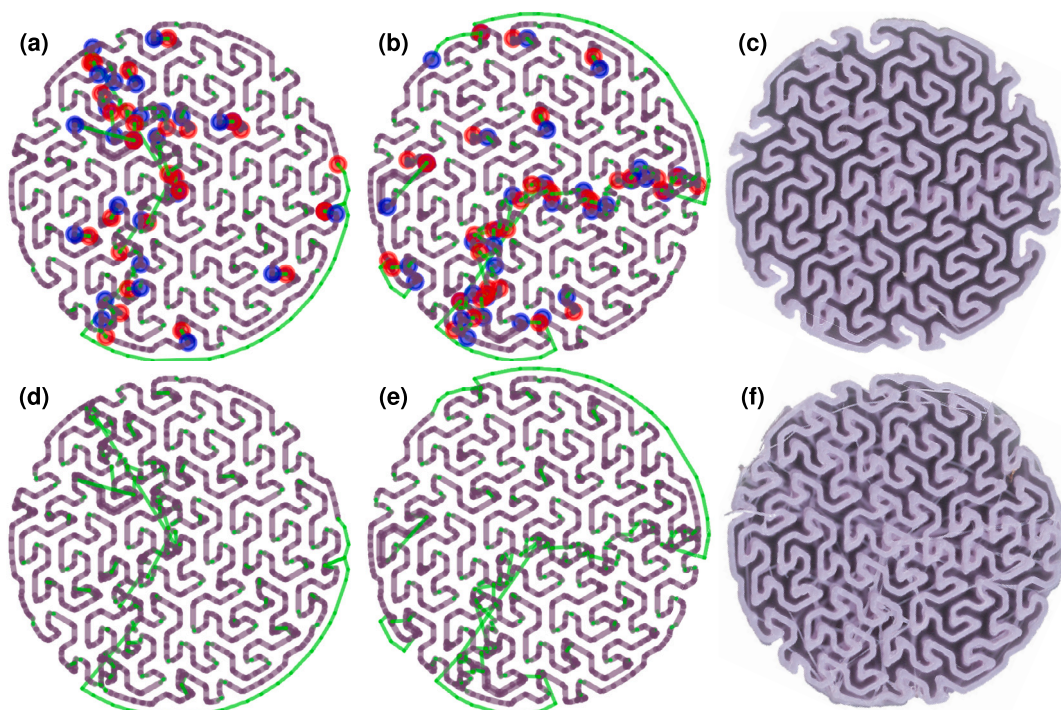


Fig. 3. Purple ABS samples; slicer: *UltiMaker Cura*; 3D printer: *FlashForge Creator PRO* (0.4 mm nozzle). G-code visualisations with green lines showing the nozzle paths at different heights, i.e. at (a, d) 15 mm and (b, e) 33 mm, as well as (c, f) top views of the corresponding samples 3D printed with: (a, b, c) retraction enabled and marked by red dots (blue dots indicate restart points, the green line is the nozzle travel path), or (d, e, f) retraction disabled.

ing other parameters such as nozzle temperature, we obtained samples with various amount of fibres in the slits, resulting from uncontrolled (in fact, random or poorly controlled) filament stringing that we deliberately provoked.

Figs. 3 and 4 show G-code visualisations at two different printing heights visualised by *gCodeViewer* [30], as well as top faces of the corresponding samples 3D printed from purple filament using a 0.4 mm nozzle. The green lines show the nozzle path, while the red dots indicate extrusion stop, and the blue ones, restart. Filament stringing and some other defects in FFF are due to inaccuracies at extrusion stops and starts. This is because precise synchronization between motion control and extrusion is required, which is a challenge due to the non-linearity of the flow inside the nozzle. Usually, this effect is compensated for on modern

machines, sometimes during the slicing and toolpath generation but also mechanically. However, plastic may often leak from the nozzle after the extruder is moved to a new location (a behaviour known as oozing), and small strings (whiskers, hairs) of polymer are left behind on a 3D printed model resulting in a “hairy” print out [9,31]. The stop and restart locations are independently placed by the specific slicer used to produce the G-code files from the CAD model in STL format. Nonetheless, their position and density are relatively uniform and can be tuned by selecting appropriate values for relevant settings such as extruder temperature and retraction distance. Retraction is the main technique used to prevent oozing when travel moves cannot be avoided [32]. It consists in a reversed feeder movement that subtracts material from the nozzle to avoid leakage. The G-code generated by the *FlashPrint 5* slicer has many

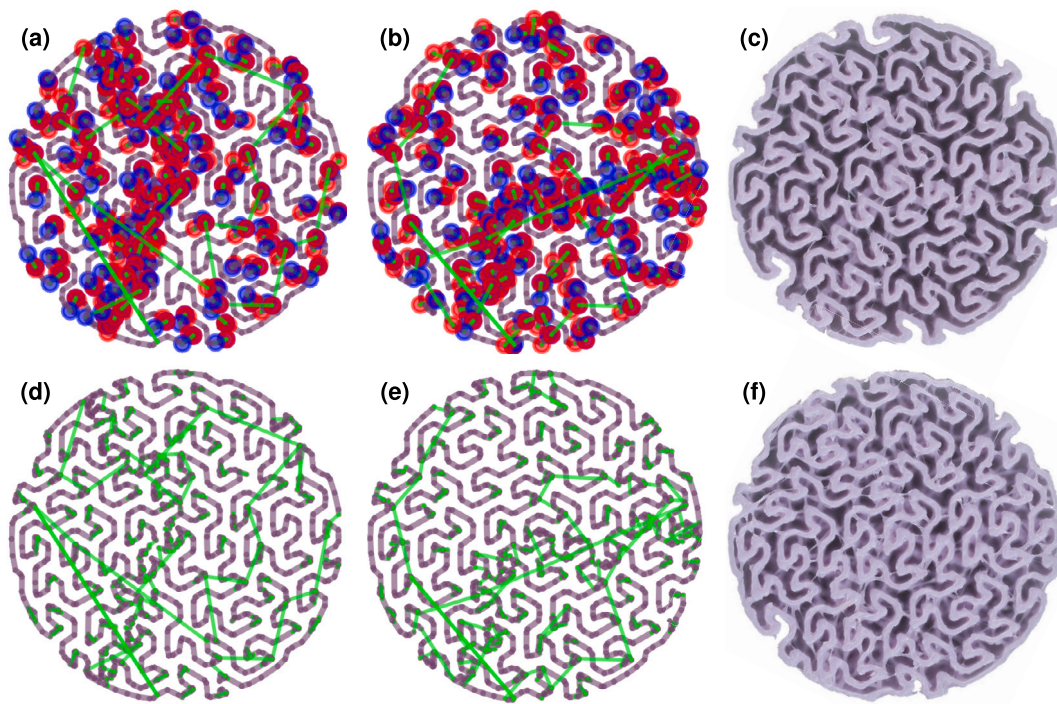


Fig. 4. Purple ABS samples; slicer: *FlashPrint 5*; 3D printer: *FlashForge Creator PRO* (0.4 mm nozzle). G-code visualisations with green lines showing the nozzle paths at different heights, i.e. at (a, d) 15 mm and (b, e) 33 mm, as well as (c, f) top views of the corresponding samples 3D printed with: (a, b, c) retraction enabled and marked by red dots (blue dots indicate restart points, the green line is the nozzle travel path), or (d, e, f) retraction disabled.

more stop and restart points at any level than the code generated by *UltiMaker Cura*, cf. Figs. 4 (a, b) and 3 (a, b), respectively. Therefore, when retraction is disabled, *FlashPrint 5* causes more fibres in the slits, see Fig. 4 (f), than *UltiMaker Cura*, see Fig. 3 (f). Moreover, fibre-free printing was achieved using *UltiMaker Cura* with retraction, see Fig. 3 (c) and also cf. Figs. 2 (e, f) with 2 (c, d). On the other hand, some filament stringing still occurred despite retraction when *FlashPrint 5* was used, see Fig. 4 (c). We expect that fibres should improve the acoustic properties of 3D printed materials. Therefore, we have decided to use *FlashPrint 5* to investigate another mechanism of fibre formation, and print the blue and red samples with the same retraction but using a higher nozzle temperature, which should result in oozing and creation of fibres.

2.3. 3D printing slotted samples with fibrous fillers using controlled stringing

Finally, a third approach was investigated, i.e. the direct design and manufacture of strings by fully controlled stringing. Direct design of the 3D printing toolpath allows structures to be created that would be impossible through the conventional approach of creating a CAD model and using slicing software to identify the toolpath for each layer [26]. In the approach proposed in this study, each layer is formed by combining two completely different printing strategies, namely: (i) a conventional technique to print the main construct, i.e. the slotted surface, using an optimised printing path that follows the PGC, and (ii) a novel approach to deliberately create thin strings by bringing the printing nozzle into contact with an auxiliary perimeter structure before quickly moving it across the main construct to lay down a thin drawn fibre. The printing speed for the strings is almost one order of magnitude higher than the speed used for the main structure, see Table 1. For the second strategy, the fibre diameter is in the region of one-tenth of the nozzle diameter [26]. Since the fibre is so small, it can be directly printed over for the next layer of the ‘conventional’ printing style. The alternating deposition strategy is repeated for all layers to achieve strings throughout the whole part. This printing concept is illustrated in Figs. 5 and 6 (a, b).

Whilst the strings created by direct toolpath design may be similar in size to those created accidentally by slicer-generated toolpaths, the direct-design approach provides full control in creating highly regular fibre fillers. It also offers opportunity for innovative control and design. Importantly, this method can achieve excellent fibre uniformity, which is beneficial for modelling. On the other hand, it is also possible to achieve controlled non-uniformity. This opens up opportunities for next-generation research into novel structures and models. Minor changes to the parametric design allow the formation of strings and string distributions with a wide range of interesting properties. For example, *intra-layer control*, i.e. control applied for the fibres of the same layer, allow for: (1) increased or decreased string density per surface area, cf. Fig. 5 (b) with (c) and (d), respectively; (2) graded spatial string distribution, e.g. more strings at the edges than in the middle, see Fig. 5 (e); (3) non-parallel string orientation with regular angular variation, see Fig. 5 (f); (4) non-parallel string with random angular variation, see Fig. 5 (g); (5) graded string thickness, i.e. gradually wider on one side of the structure than on the other, see Fig. 5 (h); (6) random string thickness, see Fig. 5 (i); (7) square-grid instead of triangular grid fibre pattern, see Fig. 5 (j); (8) discrete string positioning, e.g. with an open hole in the fibrous layer, see Fig. 5 (k). Finally, by using *inter-layer control*, the degrees of randomness or controlled non-uniformity and ratio of multi-material constituents can easily be gradually transitioned across the height of the construct.

In this study, we applied fully controlled stringing to fabricate uniform fibrous fillers inside the slits of the PGC-based material. We used the *intra-layer control* to investigate the effect of increasing the density of strings (per layer surface) on the acoustic properties of such fibre-filled slotted materials. For this purpose we used *FullControl GCode Designer* [26,33], a Python-based parametric design framework specifically tuned for Material Extrusion processes. Similarly to *Grasshopper3D*, the algorithms developed in *FullControl GCode Designer* allows the user complete freedom in toolpath generation and meticulous control of extrusion and other printing parameters during manufacturing. The approach utilises the same continuous PGC-based toolpaths

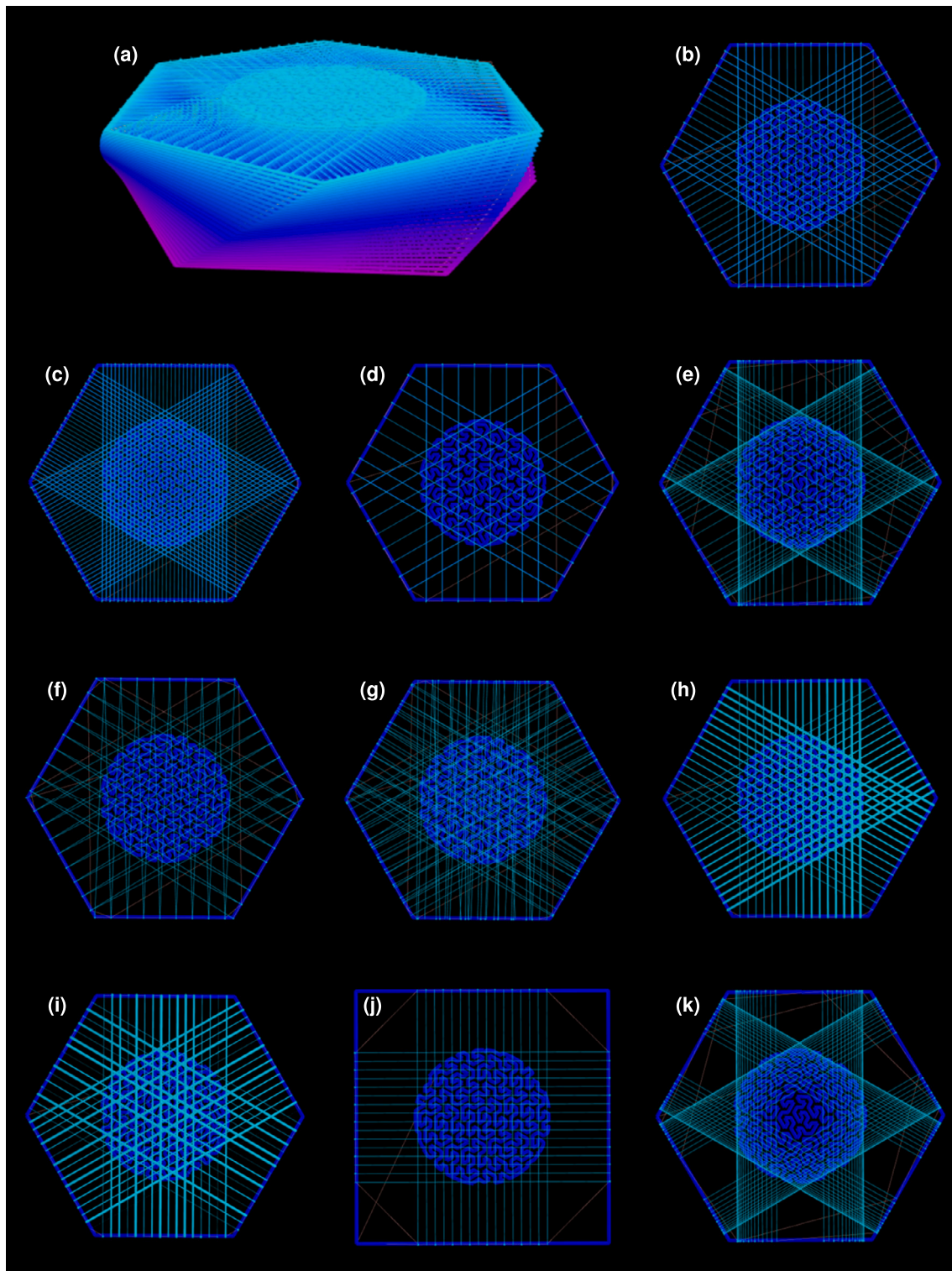


Fig. 5. (a) Overall printing strategy with strings printed across the object within an outer frame. (b,c,...,k) Top-views of example design variants achievable with controlled string placement using *FullControl GCODE Designer*: (b) default example, (c) denser strings, (d) less dense strings, (e) graded strings positioned towards the edges of the object, (f) non-parallel strings, (g) semi-randomly oriented strings, (h) graded string diameter, (i) random string diameter, (j) square unit cell instead of triangular/hexagonal, (k) discrete positioning with open central hole.

as the fibre-free designs (i.e. with a 0.6 mm nozzle and a 0.45 mm layer height). However, after printing each layer, an external hexagonal frame is printed and long horizontal strings are drawn across it over the PGC-based construct. Fig. 6 (a, b) illustrates this approach for two implemented cases, namely with: (a) $3 \times 10 = 30$ strings, and

(b) $3 \times 20 = 60$ strings. The scans and photographs of “straight” and “twisted” PLA samples shown in Fig. 6 are for the second case of 60 strings per layer. The strings are produced by careful modulation of printing speed (reaching 100 mm/s) and flow rate. Their diameter is very small, so they can be effectively sandwiched between the normal

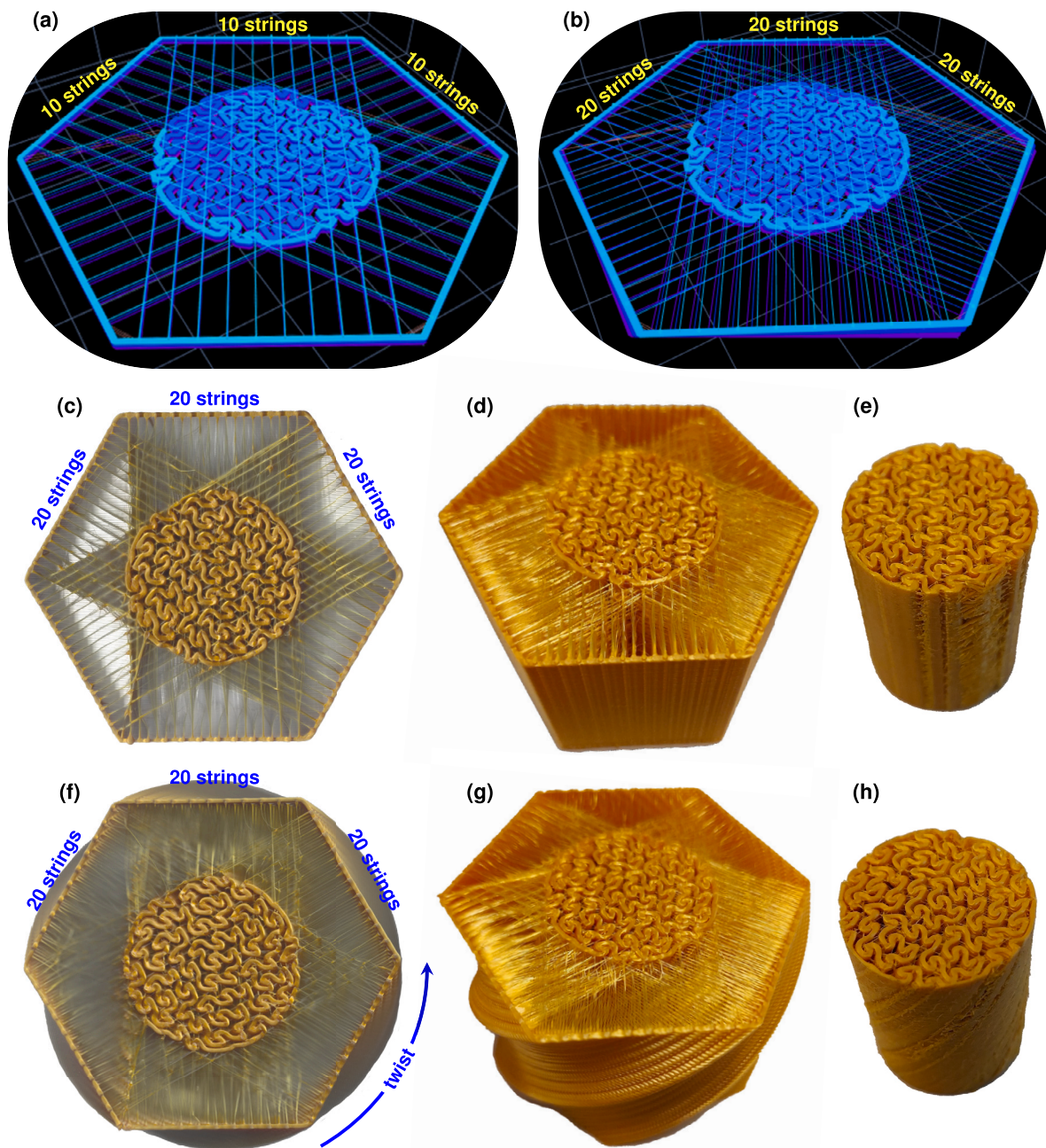


Fig. 6. Yellow PLA samples with controlled fibrous fillings; slicer: *FullControl GCODE Designer* [26,33]; 3D printer: *Creativity Ender-3* (0.6 mm nozzle). G-code visualisations for cases with (a) 30 and (b) 60 strings per layer. Scans (top views) and photographs of (c, d, e) “straight” and (f, g, h) “twisted” PLA samples with 60 strings per layer.

layers of the PGC-based design and thus locked in place within the structure, which means that the strings are regularly spaced every 0.45 mm along the axis of the cylindrical sample. In the “twisted” sample, the frames with strings are rotated following the twist of the cross section while there is no frame rotation for the “straight” sample, cf. scans in Fig. 6 (f) and (c), respectively. The hexagonal frames are later removed along with excess strings outside the sample, cf. Fig. 6 (d, g) and (e, h).

2.4. Examination of 3D printed samples

Fig. 7 presents the top faces of 3D printed samples and their zoomed details. Only “straight” samples are compared since they are more suitable for visual inspection of fibres created in their slits. However, the

observations for “straight” samples also apply to their “twisted” counterparts.

Let us first recall that it is possible to 3D print materials with complex and irregular slit patterns correctly, i.e. without fibres in the slits, see Fig. 7 (a, g), using a conventional slicer software with retraction enabled, or even a CAD software that can be used to generate an optimised G-code, provided that printing parameters, in particular temperatures and speeds, are set to the adapted values in relation to the material and printer used. Note that the effect of nozzle size is clearly visible from the comparison of the fibre-free samples: the yellow sample shown in Fig. 7 (g) was printed with a 0.6 mm nozzle and has thicker walls than the samples printed with a 0.4 mm nozzle.

The main subject of this research are slotted materials with fibres in the slits. Visual examination of such material samples allows for the following observations. As expected, fibres are produced when the re-

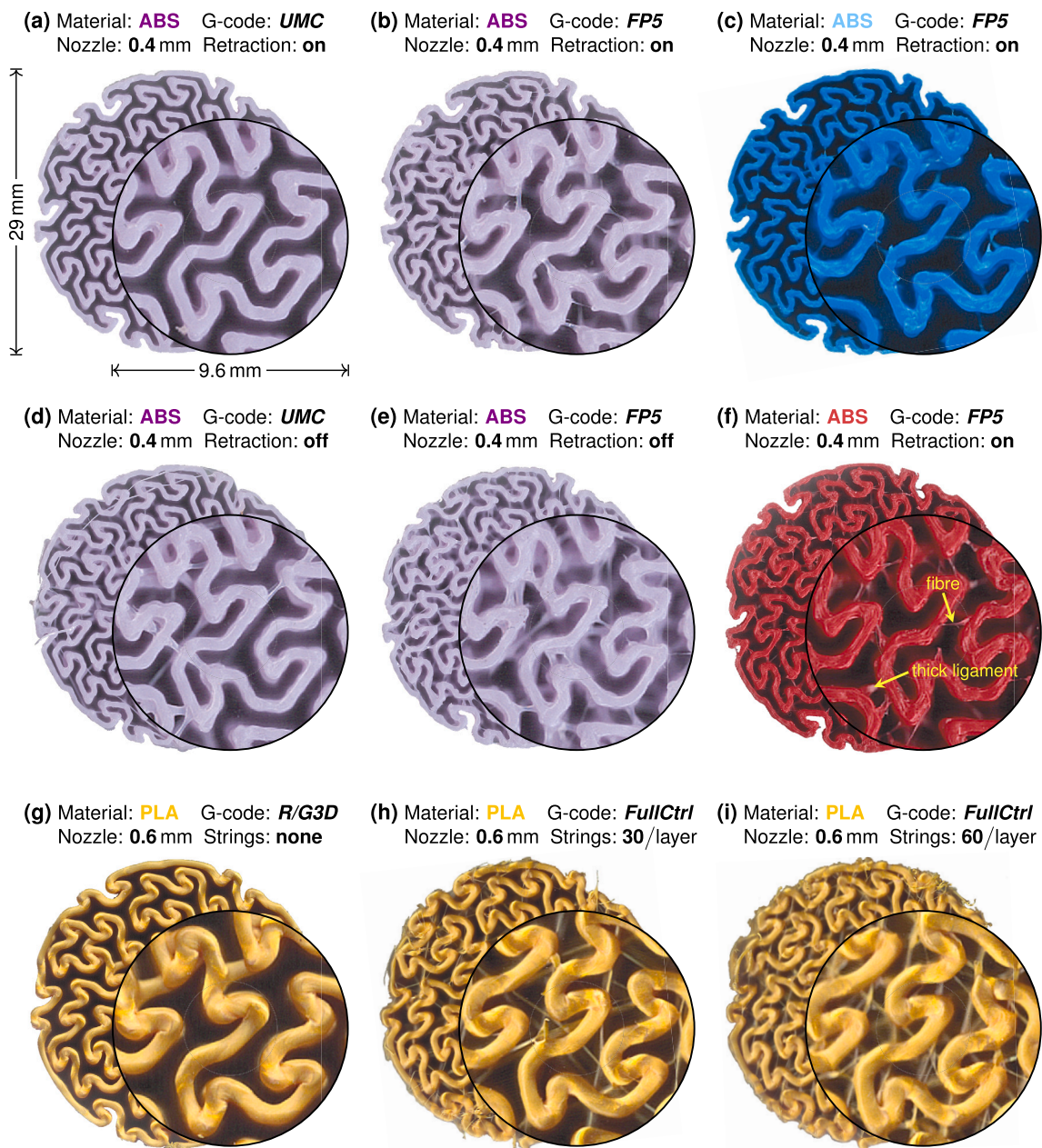


Fig. 7. Morphology of 3D printed samples.

traction function is disabled in the conventional slicer software, see Fig. 7 (d, e). Samples manufactured using *FlashPrint 5* have more fibres in the slits, because this slicer generated many retract points at each printing layer, cf. Figs. 4 and 7. Moreover, fibres are created even when this slicer is used with the retraction function turned on, see Fig. 7 (b, c, f), especially if the printing temperature is higher than required. These fibre creation methods, which can be used with conventional slicer software, usually result in a rather chaotic fibre distribution: the fibres are randomly arranged, have irregular thickness, shapes and lengths. Moreover, fibre bundles and thicker ligaments are often formed, see Fig. 7 (e, f). Although more regular fibre patterns can also be created, cf. Fig. 7 (d), they cannot be directly customised either. Modelling such heterogeneous fibre arrangements is also more problematic. These problems are overcome when fibres in the slits are precisely designed using *FullControl GCODE Designer* [26,33]: the fibres are very thin, straight, and their number (in the volume of the material) and arrangement are precisely known from the G-code, which can be confirmed by visual inspection, see Fig. 7 (h, i).

3. Mathematical model for calculating acoustic properties for slotted materials with fibrous fillers

3.1. Semi-analytical calculation of macro-parameters

The geometry of the materials 3D printed for this study is based on essentially two-dimensional patterns of slits. It is therefore possible to propose a semi-analytical way of modelling the acoustic behaviour of such materials, assuming that their skeletons are perfectly rigid and impermeable, which is the case with these 3D printed samples. This means that the carrier of acoustic waves is air saturating the open network of slits, and equivalent fluid models can be used to analyse sound wave propagation in such materials. The most rigorous models of that kind are based on the two-scale asymptotic method of homogenisation [34,35]. They are computationally efficient when using well-established scaling functions that require only a few macro-parameters such as porosity, tortuosity, permeability, characteristic lengths, etc., which are determined from the microstructure of the pore (or slit) network [35–37].

Essentially, these are well-known and measurable transport parameters in porous media [35,38]. Here, we propose a procedure for the semi-analytical calculation of the said macro-parameters of the 3D printed cylindrical samples with a pattern of winding slits running “straight” along the axis of the cylinder.

First, the face of the sample is scanned or photocopied (with a flatbed scanner) which delivers an accurate shape of the actual pattern 3D printed using a specified device and material. Then, the fluid domain of the sample inside the circular shape (defining the interior of the impedance tube) is extracted from the scan using image processing software. This domain is meshed with finite elements using the Delaunay triangulation algorithm. Numerical integration based on this mesh is used to calculate the surface area A_F of the fluid domain inside the circular tube of radius $R = 14.5$ mm, as well as the length of the total boundary of the fluid domain, i.e. the total length L_w of the (wetted) solid walls including the skeleton boundaries and the inner wall of the tube. For “straight” samples with pattern extruded parallel to their height and with ideally flat walls of the slits, the porosity is calculated as $\phi = A_F/(\pi R^2)$, and the viscous and thermal characteristic lengths, Λ_v and Λ_t , respectively, are both equal to the half of the hydraulic diameter, i.e. $\Lambda_v = \Lambda_t = 2A_F/L_w$. Finally, the Poisson problem for thermal diffusion in the fluid domain is solved using the finite element method, and the result, i.e. the scaled temperature field, is used to determine the so-called static thermal tortuosity α_{0t} and permeability Θ_0 , see Appendix A for details. For samples with slits with perfectly flat walls parallel to the sample height, the thermal permeability Θ_0 is the same as the classical Darcy permeability, i.e. the static viscous permeability \mathcal{K}_0 , when the acoustic wave propagation and the associated oscillatory flow direction are along the sample height. Consequently, also the static viscous tortuosity α_{0v} is equal to its thermal counterpart α_{0t} .

3.2. Tortuosity

Tortuosity is an important feature of the pore network [39,40] that has a strong influence on the sound absorption of air-saturated porous materials [38]. For example, by increasing tortuosity, absorption peaks related to the quarter-wavelength resonances can be shifted towards lower frequencies [41]. The tortuosity for “straight” samples (without fibres) should theoretically be unity which, in fact, means no tortuosity at all. This is the case of straight channels or slits with perfectly flat walls. However, the walls of the 3D printed samples are not particularly flat and the actual value of tortuosity is slightly higher than one (we propose a small correction below). This is also due to the internal joints that reinforce and hold the sample together and imperfections such as surface bulges deeper in the slits, therefore not captured when scanning the sample surface.

By twisting the slit pattern around the axis of the cylindrical CAD model of “twisted” samples, the tortuosity of the pore network is increased. This can be controlled by the total twist angle Ω , i.e. the angle defined with respect to the entire height of the sample, see Section 2.1 and Fig. 2 (h). We postulate that the tortuosity of “twisted” samples with a slit pattern based on the Gopser curve can be estimated as the tortuosity of an equivalent helical channel obtained by twisting a cylindrical channel (with a small diameter comparable to the slit width) around a vertical axis parallel to it, see Fig. 2 (h). The cylindrical channel is located at some distance R_h from the axis. After twisting, it becomes a helical channel with (large) radius R_h and pitch (i.e. the height of one complete helix turn) equal to H_h , with $H_h/H = 2\pi/\Omega$. The tortuosity of a helical channel can be calculated as the quadratic ratio of its length L_h to its pitch H_h . Since $L_h = \sqrt{H_h^2 + (2\pi R_h)^2}$, the helical channel tortuosity equals $(L_h/H_h)^2 = 1 + (2\pi R_h/H_h)^2$. Based on this postulate, we propose the following relation for the tortuosity α_∞ of the PGC-based slotted samples, both “straight” and “twisted” along the height, namely $\alpha_\infty/(1 + c_\alpha) = 1 + (2\pi R_h/H_h)^2$.

Here, c_α is a small arbitrary correction of tortuosity accounting for bumpy walls (surface bulges) and internal joints, while $R_h = \xi_h R$ and $H_h = 2\pi H/\Omega$ are the radius and height of the equivalent helical channel, respectively. For slits running from the centre to the edge of the sample, the reasonable radius of the helix should be slightly larger than half the radius of the sample and we found that $\xi_h = R_h/R \approx 0.6$ ensures good matching for the twisted PGC-based slits. This original approach to estimate the tortuosity of twisted slits is discussed in more detail in Appendix B. Note that for samples with “straight” slit patterns, i.e. when $\Omega = 0$, we have $H_h \rightarrow \infty$ and $\alpha_\infty = 1 + c_\alpha$, which means that only a small tortuosity correction c_α for non-perfectly flat walls of the slits is then applied. We assumed $c_\alpha = 0.05$ for the 0.4 mm nozzle and 0.10 for the 0.6 mm nozzle, as the slit walls are more bumpy with larger nozzle and layer thickness. The problem of imperfect slits with unintended variable width in slotted acoustic materials manufactured by FFF technology was reported by Opiela et al. [42]. It has been recently addressed by Attenborough [43], who has also proposed formulas for tortuosity in the case of regularly periodically varying slit widths.

How tortuous the pore fluid network is, especially if it is high, strongly affects the fluid flow through it. This is reflected in the static viscous permeability. For oblique or tortuous channels or slits the following formula can be applied

$$\mathcal{K}_0 \approx \Theta_0/\alpha_\infty = \phi\Psi_0/\alpha_\infty. \quad (2)$$

See Appendix B for the definition of Ψ_0 . This simple estimate proved to be very accurate. For consistency, the static viscous tortuosity is also modified, namely $\alpha_{0v} \approx \alpha_\infty \alpha_{0t}$, which ensures the condition $\alpha_{0v} > \alpha_\infty$.

3.3. Dynamic permeabilities

The frequency-dependent dynamic permeabilities for thermal and viscous effects can be determined using the well-known Johnson-Champoux-Allard-Lafarge-Pride (JCALP) model [44–47]

$$\Pi_\omega(\Pi_0, \mathcal{M}, \mathcal{P}, \omega_c) = \Pi_0 \left(\frac{i\omega}{\omega_c} + 1 - \mathcal{P} + \sqrt{\mathcal{P}^2 + \frac{\mathcal{M}}{2} \frac{i\omega}{\omega_c}} \right)^{-1}, \quad (3)$$

where $\omega = 2\pi f$ is the angular frequency (f is the ordinary frequency) and i is the imaginary unit. The scaling function (3) depends on the corresponding static permeability Π_0 (i.e. the value of Π_ω at $\omega = 0$), two shape factors, \mathcal{M} and \mathcal{P} , and a characteristic frequency ω_c , which are calculated for thermal and visco-inertial effects as specified below, using the respective macro-parameters determined in Sections 3.1 and 3.2.

Let us first consider the thermal effects. The corresponding dynamic thermal permeability [46,38,37] is calculated as

$$\Theta(\omega) = \Pi_\omega(\Theta_0, \mathcal{M}_t, \mathcal{P}_t, \omega_t), \quad (4)$$

where the thermal shape factors and characteristic frequency are

$$\mathcal{M}_t = \frac{8\Theta_0}{\phi\Lambda_t^2} = \frac{8\Psi_0}{\Lambda_t^2}, \quad \mathcal{P}_t = \frac{\mathcal{M}_t}{4(\alpha_{0t} - 1)} = \frac{2\Psi_0/\Lambda_t^2}{\alpha_{0t} - 1}, \quad \omega_t = \frac{\phi \tau_a}{\Theta_0} = \frac{\tau_a}{\Psi_0}, \quad (5)$$

and τ_a is the thermal diffusivity of air saturating the pores, or in this case, slits. Similarly, visco-inertial effects are taken into account through the dynamic viscous permeability [44,47,38,37]

$$\mathcal{K}(\omega) = \Pi_\omega(\mathcal{K}_0, \mathcal{M}_v, \mathcal{P}_v, \omega_v), \quad (6)$$

where the viscous shape factors and characteristic frequency are

$$\mathcal{M}_v = \frac{8\mathcal{K}_0\alpha_\infty}{\phi\Lambda_v^2}, \quad \mathcal{P}_v = \frac{\mathcal{M}_v}{4(\alpha_{0v}/\alpha_\infty - 1)}, \quad \omega_v = \frac{\phi \nu_a}{\mathcal{K}_0\alpha_\infty}. \quad (7)$$

Here, ν_a is the kinematic viscosity of air. Note that due to the estimated formulas for macro-parameters proposed above, the corresponding viscous and thermal shape factors are identical, i.e. $\mathcal{M}_v = \mathcal{M}_t$ and $\mathcal{P}_v = \mathcal{P}_t$, while $\omega_v \approx \nu_a/\Psi_0 = \omega_t N_a$, where N_a is the Prandtl number of air.

3.4. Effective properties

The dynamic permeabilities allow to determine the effective properties of the equivalent fluid used to model acoustic behaviour of a porous material with a rigid frame [38,37]. The frequency-dependent effective compressibility of such a medium is

$$C(\omega) = \frac{\phi}{P_a} \left(1 - \frac{\gamma_a - 1}{\gamma_a} \frac{\Theta(\omega)}{\phi \tau_a} i\omega \right), \quad (8)$$

where P_a is the ambient mean pressure and γ_a is the heat capacity ratio of the fluid, i.e. air, saturating the pore network (or in this case, the network of slits). Now, the effective density $\rho_e(\omega)$ and speed of sound $c_e(\omega)$ are determined as follows

$$\rho_e(\omega) = \frac{\eta_a}{i\omega \mathcal{K}(\omega)}, \quad c_e(\omega) = \frac{1}{\sqrt{\rho_e(\omega) C(\omega)}}, \quad (9)$$

where η_a is the dynamic viscosity of air. These effective properties can be used in particular to solve the Helmholtz acoustics problem to determine the sound absorption by a material exposed to plane acoustic waves incident perpendicularly to its surface.

3.5. Correction for fibres in the slits

The fibres formed by filament stringing in the pores or slits can be thought of as fibrous fillers in the pore network of the enhanced acoustic composite thus created. These fibrous fillers are acoustic materials in themselves and can be modelled as an equivalent fluid that is fundamentally different (because the fibrous materials are lossy and dispersive) from the air filling the space around the fibres. Here we propose a simple yet sufficient way of such modelling.

Let ϕ_f be the porosity of the fibrous filler. For many porous materials, the tortuosity can be well estimated on the basis of their porosity [40,38,48]. The following relationship between tortuosity and porosity [40,49] is often quite accurate for highly porous materials

$$\alpha_{\infty f} = \sqrt{2 - \phi_f}. \quad (10)$$

Many formulas of this kind have been derived or proposed for various porous media [40], and we have verified that other well-known relationships, e.g. $\alpha_{\infty f} = \sqrt{1 - \ln \phi_f}$, can also be applied for the stringing-based fibrous fillers of this study without significant changes in the final sound absorption results of such modelling. In particular, also the formula $\alpha_{\infty f} = 2 - \phi_f$ that is valid for cylindrical fibres perpendicular to flow direction [50] can be used for purple ABS and yellow PLA samples with high-porosity fillers of regular fibres. All this suggests that only one parameter discussed below should be of key importance in modelling and it is not either of the parameters ϕ_f and $\alpha_{\infty f}$, which are close to unity for highly porous fibrous materials.

Acoustic fibrous materials usually have high porosity, and the presence of fibres mainly introduces the viscous dissipation of acoustic wave energy due to viscous drag forces caused by the oscillatory flow of fluid (air) around the motionless fibres, while thermal effects can be neglected. To evaluate the influence of viscous dissipation effects on wave propagation in fibrous materials, the viscous characteristic length Λ_{vf} is required. A simple formula to estimate this length for fibrous materials was proposed by Allard [38] (Chapter 5.3.4, page 81) and it can be rewritten as follows

$$\Lambda_{vf} = (2\pi R_f L_f / V_f)^{-1} = \frac{1}{2\pi \mathcal{L}_f}, \quad \mathcal{L}_f = R_f \frac{L_f}{V_f}, \quad (11)$$

where R_f is the radius of the fibres and L_f is the total length of the fibres in the representative volume V_f . Here, we have introduced a useful geometric parameter \mathcal{L}_f that combines these quantities.

Now, the static viscous permeability \mathcal{K}_{0f} can be estimated for a fibrous material, while the viscous characteristic frequency ω_{vf} is calculated in a standard way, namely

$$\mathcal{K}_{0f} = \frac{\phi_f \Lambda_{vf}^2}{8\alpha_{\infty f}}, \quad \omega_{vf} = \frac{\phi_f v_a}{\mathcal{K}_{0f} \alpha_{\infty f}} = \frac{8v_a}{\Lambda_{vf}^2}. \quad (12)$$

The corresponding dynamic viscous permeability is determined as

$$\mathcal{K}_f(\omega) = \Pi_\omega(\mathcal{K}_{0f}, 1, 1, \omega_{vf}), \quad (13)$$

using the Johnson-Champoux-Allard (JCA) model [44,45,38] obtained from the JCALP model (3) for $\mathcal{P} = 1$. The effective density for an equivalent fluid that can replace the fibrous material, equals

$$\rho_f(\omega) = \frac{\eta_a}{i\omega \mathcal{K}_f(\omega)}. \quad (14)$$

The simplest formula for the equivalent viscosity is $\eta_f = \eta_a / \phi_f$ which can be assumed for fibrous materials with higher porosities and accounts for the increase in viscosity due to the presence of motionless fibres. Now, the kinematic viscosity for such an equivalent fluid can be calculated as

$$\tilde{\nu}_f(\omega) = \frac{\eta_f}{\rho_f(\omega)} = \frac{i\omega \mathcal{K}_f(\omega)}{\phi_f}. \quad (15)$$

This effective kinematic viscosity replaces v_a in the formula for ω_v shown in Equation (7), so that the dynamic viscous permeability $\mathcal{K}(\omega)$ of the acoustic composite with fibrous fillers in the slits is determined as follows

$$\mathcal{K}(\omega) = \Pi_\omega(\mathcal{K}_0, \mathcal{M}_v, \mathcal{P}_v, \tilde{\omega}_v), \quad \tilde{\omega}_v = \frac{\tilde{\nu}_f}{\Psi_0}. \quad (16)$$

For simplicity, and especially for highly porous fillers, the effective properties of the acoustic slotted material with fibres in the slits can be calculated as in Section 3.4. Finally, it is important to notice that $\tilde{\nu}_f \rightarrow v_a$ when $\phi_f = 1$ and $\mathcal{L}_f \rightarrow 0$, i.e. when there are essentially no fibres in the slits, and then $\tilde{\omega}_v \rightarrow \omega_v$, which leads back to the original model presented in Section 3.

4. Sound absorption by 3D printed materials: discussion of experimental and modelling results

4.1. Results for slotted samples with fibres formed by uncontrolled stringing

Fig. 8 shows sound absorption determined experimentally for all purple ABS samples, using a 29 mm impedance tube [51], see Fig. 2(g). Comparison of the absorption curves measured for “straight” samples, see Fig. 8(a), leads to the following observations and conclusions. As expected, sound absorption is better in the entire frequency range when there are fibres in the slits. As shown in Section 2.4, fibres can be produced by turning off retraction and thus inducing oozing. However, when using the *FlashPrint 5* slicer software, fibres were produced even with retraction, and the corresponding improvement in sound absorption is comparable to that obtained using the *Ultimaker Cura* slicer with retraction disabled. Therefore, the best improvement in sound absorption is achieved for samples produced using the *FlashPrint 5* slicer with the retraction distance set to zero (i.e. disabled). The results obtained for samples with a twisted slit pattern, see Fig. 8(b), confirm these observations even more clearly: not only the sound absorption of the “twisted” samples is better – as expected – than that measured for their “straight” counterparts, but the improvement in absorption due to the fibres in the slits is more significant. This is mainly because the path of the oscillatory flow induced by acoustic waves penetrating the slotted material is longer when the slits are twisted, so that the interaction with the fibres in the slits and the corresponding viscous losses become more significant. Incidentally, the small isolated peaks at about 4.3 kHz in Fig. 8(a) and 3.9 kHz in Fig. 8(b) are measurement artefacts.

Sound absorption measurements were used to validate the mathematical model discussed in Section 3. This semi-analytical modelling requires the numerical solution of the Poisson problem for thermal diffusion inside a slit network as shown in Appendix A for the purple sample. The same calculation procedure was also applied for other samples and

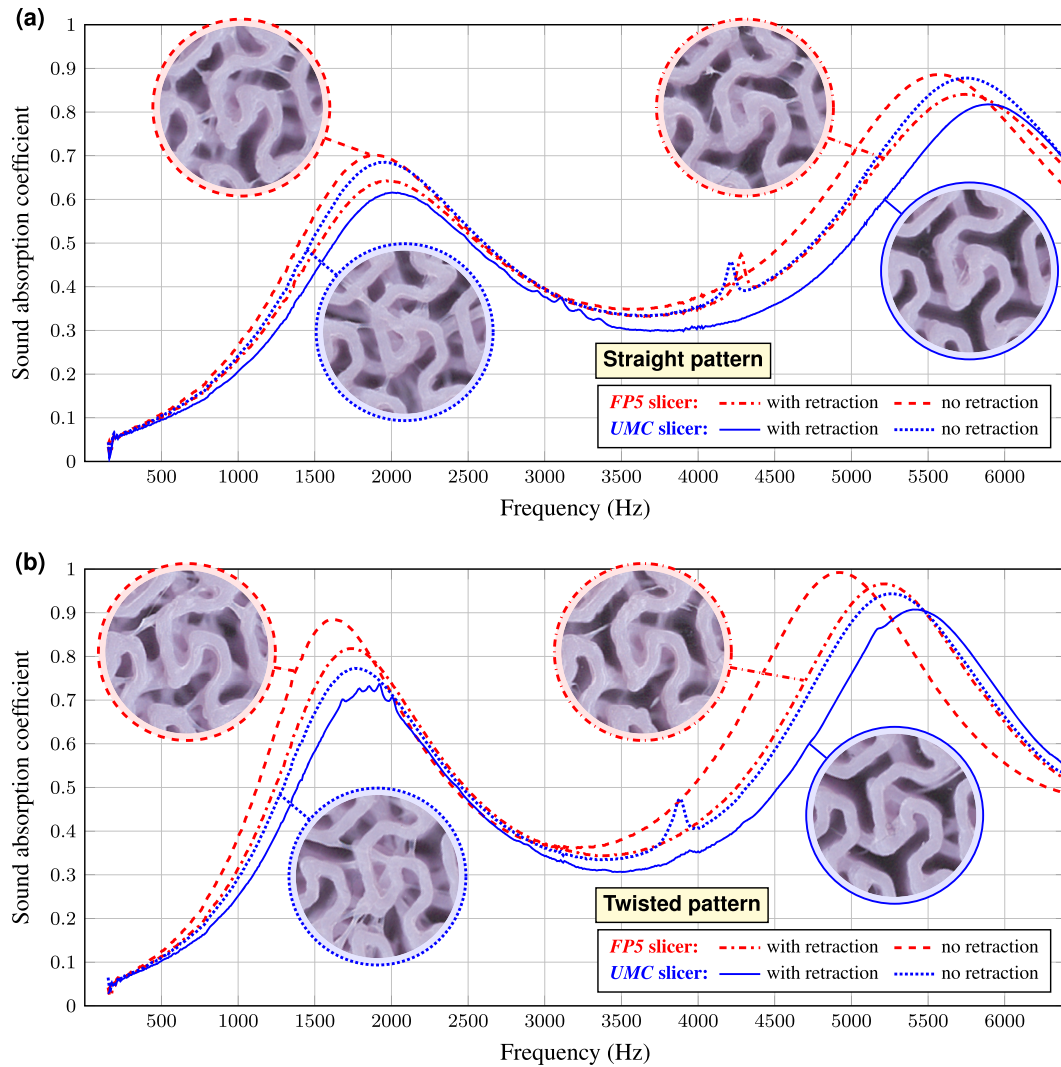


Fig. 8. Experimental results: sound absorption measured for purple samples.

all parameters determined in that way – including those calculated analytically in particular for the “twisted” samples – are listed in Table 2. Note that the macro-parameters for the purple samples differ from those determined for the blue and red samples (printed at a temperature 10°C higher), while those for the yellow samples (printed with a larger nozzle) are even more different. Table 2 also shows parameters calculated using the cross-section of the CAD model that was used to print samples, see Fig. 2(a). When comparing the tortuosity values in Table 2, one should notice that the gain in tortuosity due to twisting is 0.15 (see also Appendix B) and this value is consistently increased to 0.16 by the small tortuosity correction. It is the same for all samples because the twist angle Ω is the same in each case.

The parameters from Table 2 are sufficient to make acoustic predictions for slotted materials *without* fibres in the slits. To account for the effect of fibres, two additional parameters are required, namely ϕ_f and \mathcal{L}_f . Reasonable estimates for these two parameters are given in Table 3 – for all, i.e. purple, blue, red and yellow samples – along with the three resulting parameters calculated using ϕ_f and \mathcal{L}_f and formulas given in Section 3.5, which provide typical values for fibrous materials. The values for purple samples show that quite similar amounts of fibres are produced in the filament stringing process when using the UMC slicer with retraction turned off ($d_{\text{ret.}} = 0$) and the FP5 slicer with retraction enabled ($d_{\text{ret.}} = 1.3\text{ mm}$), cf. also Fig. 7 (b) and (d).

The determined effective properties of acoustic materials with straight and twisted slit patterns, with or without fibres in the slits,

enabled the calculation of the sound absorption coefficient. In Fig. 9, we compare the modelling results with the corresponding measurements for the purple samples produced using G-codes generated by the UMC and FP5 slicers. For the sake of brevity, we only present results for the extreme cases, i.e. for the “straight” samples 3D printed with retraction enabled, and the “twisted” ones 3D printed with retraction disabled. Recall that the UMC slicer with retraction enabled prevented the filament stringing, while the FP5 slicer did not, though larger amount of fibres is, of course, produced when the retraction function is turned off. Also more fibres – judging by visual inspection and the estimated total length – are formed in the twisted slits and their effect is more significant in that case. This is confirmed by the results of measurement and modelling shown in Fig. 9. The agreement of these experimental results with their corresponding predictions is good in the frequency range up to 3 kHz. It is in general satisfactory when one recalls that the modelling is based on two-dimensional representations of three-dimensional samples with irregularities in their structure caused by printing imperfections and internal joints. Such structural uncertainties as well as surface roughness are not taken into account in the modelling and cause discrepancies that would be uncommon, e.g., for conventional acoustic foams. The influence of surface roughness becomes particularly important at higher frequencies (above 3 kHz in this case) and between the absorption peaks resulting from quarter-wavelength resonances.

Table 2

Parameters for materials with slit patterns based on the PGC (recall that the “straight” case is for $\Omega = 0$ deg, and the “twisted” case is for $\Omega = 103$ deg).

3D printed sample material / nozzle / temp.	ϕ %	α_{0t} —	$\Lambda_t = \Lambda_v$ mm	Θ_0 10^{-8} m^2	Ω deg	α_∞ —	α_{0v} —	\mathcal{K}_0 10^{-8} m^2
Purple ABS / 0.4 mm / 230 °C	51.9	1.43	0.628	2.37	0	1.10	1.57	2.15
					103	1.26	1.80	1.87
Blue ABS / 0.4 mm / 240 °C	54.7	1.46	0.701	3.35	0	1.05	1.54	3.19
					103	1.21	1.77	2.78
Red ABS / 0.4 mm / 240 °C	54.8	1.46	0.674	3.22	0	1.05	1.53	3.06
					103	1.21	1.77	2.66
Yellow PLA / 0.6 mm / 200 °C	39.3	1.52	0.624	2.40	0	1.10	1.67	2.18
					103	1.26	1.92	1.90
CAD model	48.1	1.40	0.572	1.82	0	1.00	1.40	1.82
					103	1.15	1.61	1.58

Table 3

Parameters for fibrous fillers produced by uncontrolled or fully controlled filament stringing inside the slits.

3D printed sample material / nozzle / temp.	$d_{\text{ret.}}$ mm	Ω deg	ϕ_f %	\mathcal{L}_f m^{-1}	α_{cof} —	Λ_{vf} mm	\mathcal{K}_{of} 10^{-8} m^2
Purple ABS / 0.4 mm / 230 °C (UMC, retraction enabled, no fibres)	1.3	0	100	0 ^(*)	1	∞	∞
		103	100	0 ^(*)	1	∞	∞
Purple ABS / 0.4 mm / 230 °C (UMC, retraction disabled)	0	0	97.0	150	1.015	1.061	13.5
		103	96.0	200	1.020	0.796	7.45
Purple ABS / 0.4 mm / 230 °C (FP5, retraction enabled)	1.3	0	98.0	100	1.010	1.592	30.7
		103	95.0	250	1.025	0.637	4.70
Purple ABS / 0.4 mm / 230 °C (FP5, retraction disabled)	0	0	97.0	150	1.015	1.061	13.5
		103	92.0	400	1.039	0.398	1.75
Blue ABS / 0.4 mm / 240 °C (FP5, retraction enabled)	1.3	0	97.0	20	1.015	7.958	757
		103	82.0	120	1.086	1.330	16.7
Red ABS / 0.4 mm / 240 °C (FP5, retraction enabled)	1.3	0	84.6	128	1.074	1.241	15.2
		103	67.2	273	1.152	0.583	2.48
Yellow PLA / 0.6 mm / 200 °C (R/G3D, optimised G-code, no fibres)	N.A.	0	100	0 ^(*)	1	∞	∞
		103	100	0 ^(*)	1	∞	∞
Yellow PLA / 0.6 mm / 200 °C (FullCtrl, 30 strings per layer)	N.A.	0	98.8	300	1.006	0.531	3.46
		103	98.5	400	1.008	0.398	1.93
Yellow PLA / 0.6 mm / 200 °C (FullCtrl, 60 strings per layer)	N.A.	0	97.6	600	1.012	0.265	0.84
		103	97.0	800	1.015	0.199	0.47

^(*) Virtually no fibres are produced by filament stringing when using the **UMC** slicer with **retraction enabled** or generating an optimised G-code using CAD software, so the acoustic material model without fibres works well in these cases. However, we have also checked that the same results are then obtained from the composite model with $\phi_f = 100\%$ and $\mathcal{L}_f < 1 \text{ m}^{-1}$ ($\mathcal{L}_f \neq 0$ to avoid division by zero), which proves that the modelling is consistent. Formally, for no fibres in the slits: $\phi_f = 1$ and $\mathcal{L}_f = 0$, and then $\alpha_{\text{cof}} = 1$, $\Lambda_{\text{vf}} \rightarrow \infty$, and $\mathcal{K}_{\text{of}} \rightarrow \infty$.

4.2. The effect of uncontrolled stringing on sound absorption by blue and red samples

Since more fibres are produced when using *FlashPrint 5*, we deliberately used this slicer to 3D print blue and red samples. Recall that different ABS materials were used to make these samples, and the nozzle temperature was 10 °C higher than that used for the purple samples, i.e. 240 °C instead of 230 °C. As a result, more fibres appeared in the slits, especially in the case of red samples, see Fig. 7 (f) in Section 2.4, although the retraction was always enabled. A characteristic feature is that there are thin fibres as well as thick fibres and ligaments due to uncontrolled stringing caused by excessively high temperatures.

The macro-parameters calculated for the blue and red samples are given in Table 2. They are very similar which means that the surface scans for the blue and red samples are mutually representative. Reasonable estimates for two additional parameters, namely ϕ_f and \mathcal{L}_f , which

are required to account for the fibres in the slits of the blue and red samples, are given in Table 3 (along with the three parameters that were determined using ϕ_f and \mathcal{L}_f). One should notice a relatively low value of \mathcal{L}_f for the “straight” blue sample.

Fig. 10 compares sound absorption by “straight” and “twisted” blue and red samples. The overall absorption determined for the red samples manufactured with significant filament stringing is generally better than that obtained for the red samples manufactured with moderate stringing, cf. the corresponding absorption curves between graphs (b) and (a) in Fig. 10. In addition to the experimental results, two sound absorption predictions are shown for each sample: one taking into account the presence of fibres in the slits, and one based on the calculations without fibres. Both curves calculated for the “straight” blue sample (i.e. with and without fibres) are nearly identical and predict absorption that is slightly lower than the experimental result over the entire frequency

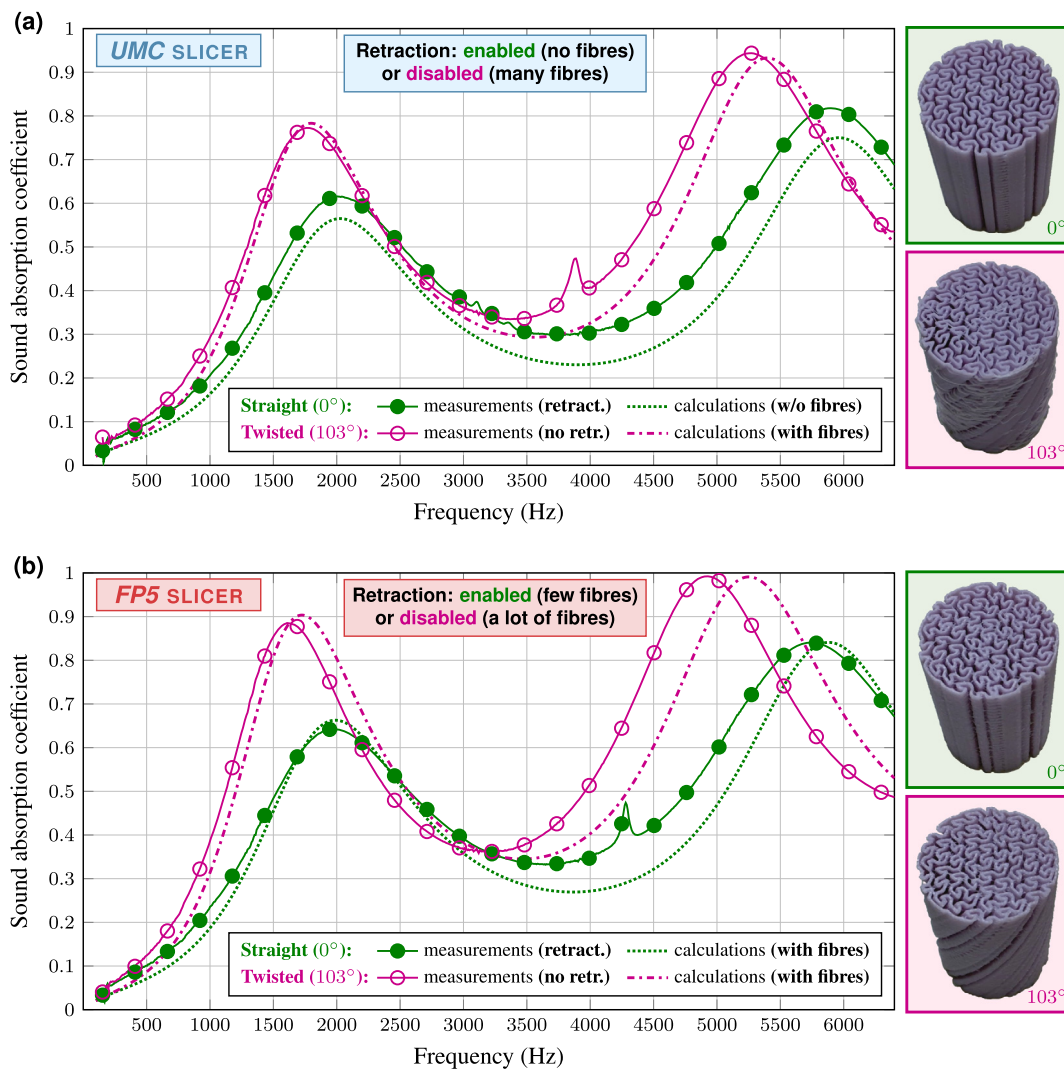


Fig. 9. Sound absorption for four purple samples: measurements and correct predictions (with acceptable discrepancies due to manufacturing imperfections).

range, see Fig. 10 (a). The low absorption between peaks is clearly underestimated, but the peak frequencies are well predicted, and the sound absorption coefficient measured there (i.e. at the peaks) is almost the same as predicted. In many studies on this topic, such a discrepancy is attributed to surface roughness [12,15,52], which is usually ignored in modelling, even though the surface roughness is quite significant in the case of materials printed using FFF technology. One may conclude that for the “straight” blue sample the acoustic model *without* fibrous fillers is sufficient to make useful, acceptable sound absorption predictions, and consequently, a criterion for taking into account the presence of fibres can be introduced: roughly speaking, for highly porous fibrous fillers, the presence of fibres can be neglected when $\mathcal{L}_f < 20 \text{ m}^{-1}$. This criterion is not met for the “twisted” blue sample, where the influence of the fibres in the slits cannot be ignored to obtain accurate sound absorption predictions, see Fig. 10 (a). The impact of fibres for acoustic absorption is even more evident from the comparison of experimental and semi-analytical results obtained for the red samples. The discrepancy between the measured sound absorption and the prediction neglecting fibres for the “straight” red sample is already unacceptably large, but it is huge for the “twisted” red sample, see Fig. 10 (b). Moreover, in both cases, the frequencies of the absorption peaks are not correctly predicted: they are shifted to clearly higher values than those found experimentally. These differences disappear when the presence of fibres is taken into account in the modelling.

4.3. Results for slotted materials with fibrous fillers printed using controlled stringing

Sound absorption was also measured and calculated for the yellow samples. Recall that these samples were 3D printed from PLA using 0.6 mm nozzle, which makes them significantly different from the ABS samples. The macro-parameters calculated from the microstructural analysis of the PLA sample are listed in Table 2. One should notice that the porosity is just below 40%, which is much lower than the porosities of the ABS samples, which are clearly above 50%. The sound absorption predictions for two yellow samples without fibres are plotted in Fig. 11 (a). They are in good agreement with the corresponding experimental results, especially with respect to the sound absorption peak frequencies, which are correctly predicted. On the other hand, sound absorption values are underestimated, in particular between the peaks, where the differences between measurements and predictions reach 0.1. As already mentioned, such discrepancies are often encountered in the case of sound-absorbing materials printed using FFF technology where the surface roughness, usually associated with the print layer thickness, plays an important role [11,12,15]. Surface roughness increases viscous dissipation effects, which are more important between the sound absorption peaks associated with quarter-wavelength resonances. Therefore, modelling that neglects roughness underestimates the absorption, especially between these resonances. Note that to some extent, these absorption curves are comparable to those obtained for the correspond-

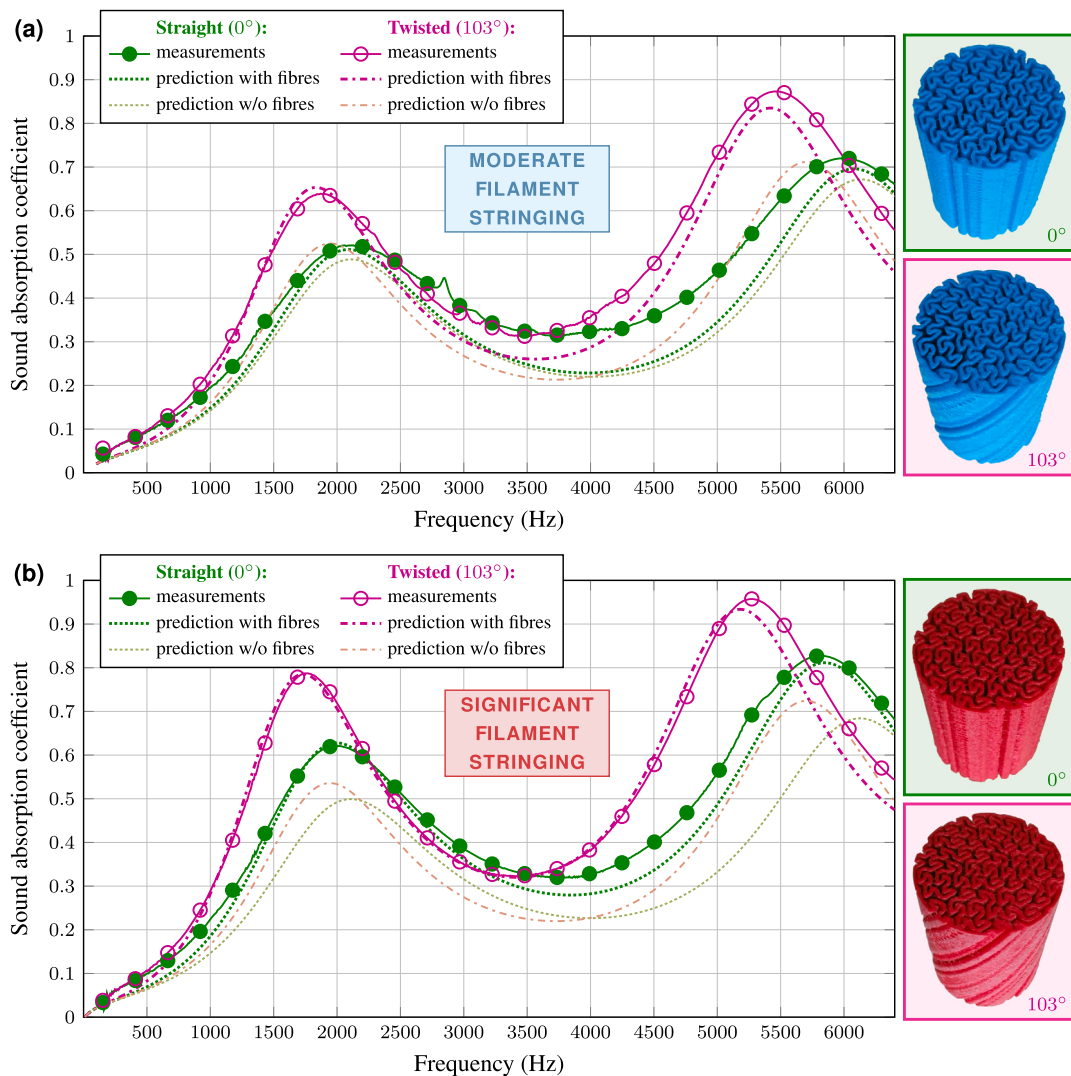


Fig. 10. Sound absorption for blue and red samples: measurements and predictions (correct for calculations with fibres and less accurate or incorrect for calculations without fibres).

ing purple samples without fibres, 3D printed using G-codes generated by the *UMC slicer* with retraction enabled, cf. experimental results in Fig. 11 (a) with solid blue curves in Fig. 8 (a, b). This is no longer valid when fibres are involved.

The sound absorption of yellow samples with fibres created using *FullControl GCODE Designer*, see Fig. 11 (b, c), is generally better than that obtained for ABS samples with fibres created in a rather uncontrolled way, despite the fact that the fibres in yellow samples were 3D printed in layers every 0.45 mm, which means three times fewer layers than in the case of ABS samples. Determining the parameters of the fibrous materials in yellow samples printed with controlled stringing was quick and simple. They are listed in the bottom four rows of Table 3. We also found that in this case the fibrous model could be reduced to only one parameter \mathcal{L}_f . This is because the effect of high porosity can be neglected assuming $\phi_f = 1$, although we used estimated values based on small weight differences between samples. Finally, it is worth noting the consistent approach, where \mathcal{L}_f for the samples printed with 60 strings per layer is twice as large as for 30 strings.

Graphs (b) and (c) in Fig. 11 show the experimental results and sound absorption predictions obtained for slotted acoustic composites with fully controlled fibres printed in the slits. The results for the “straight” samples are presented in Fig. 11 (b), and those for the “twisted” ones in Fig. 11 (c). For comparison, we also copied to each graph the corresponding sound absorption curve from Fig. 11 (a) – calculated for the

respective yellow sample without fibres – to clearly demonstrate how much can be gained by adding fibres and thus creating enhanced acoustic materials. It is easy to see that in the case of yellow samples with fibres, the absorption peaks are advantageously shifted to lower frequencies where they reach the maximum value of 1. Moreover, the overall absorption between the peaks is much higher than that obtained for other samples. Coincidentally, doubling the number of strings (from 30 to 60) has a similar effect to twisting, cf. the results marked with orange solid squares in Fig. 11 (b) with those marked with blue empty triangles in Fig. 11 (c).

5. Conclusions

We have shown that intentional filament stringing can be used to produce fibres in the slits (or pores) of 3D printed acoustic materials which leads to a significant increase in sound absorption. Strong oozing/stringing can be provoked and used to improve sound absorption of such 3D printed materials and the entire approach can be controlled and taken into account in the acoustic modelling. The amount of fibres – estimated, e.g. as their total length in a representative volume – can be controlled using standard slicer software by turning off the retraction (i.e. setting the retraction distance to zero) or by modifying its parameters, in particular the speed and retraction distance. Sometimes, acoustically useful fibres can be produced by a malfunctioning

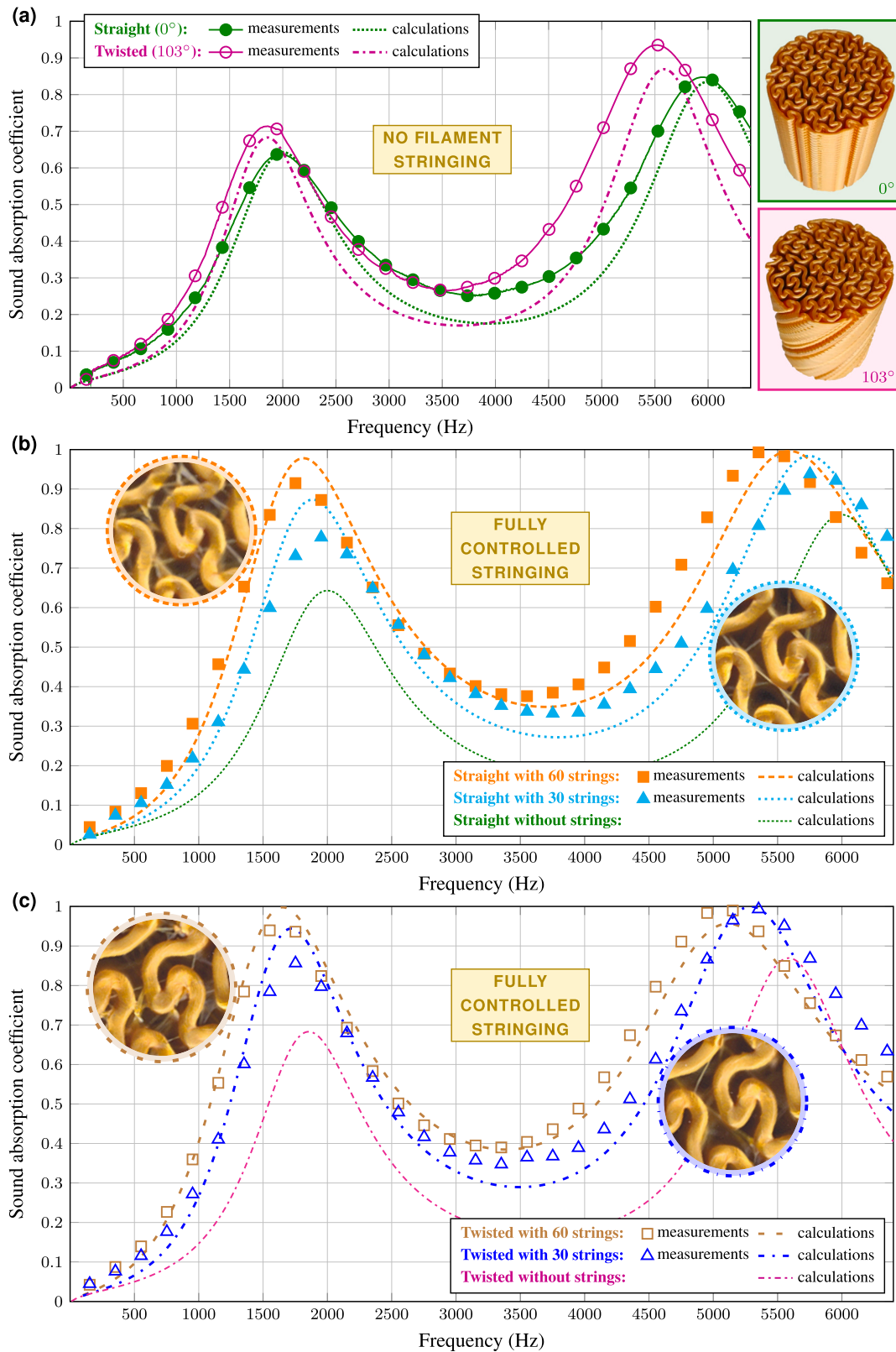


Fig. 11. Sound absorption for yellow samples: measurements and correct predictions.

slicer that generates too many retraction and restart points. Yet another method is deliberately setting incorrect values for some of the other printing parameters (e.g. temperature and speed) which is usually less predictable but opens up new possibilities. However, the approach using standard slicer software tends to provide a rather chaotic fibre distri-

butions (fibres may have irregular cross-sections, shapes and lengths, random positions, etc.), which are usually reproducible and suitable for homogenisation – as demonstrated in this work – but require at least one, directly unknown, fitting/averaging parameter. Therefore, to have more control on fibre shapes, lengths, and overall distribution,

one should use more versatile software such as *FullControl GCODE Designer* which allows to precisely design extrusion and stringing paths, control fibre diameters and positions, etc. When using this software, the actual fibre layout can be precisely designed in G-code, which can be exploited because the fibre arrangement is known to influence the acoustic properties of fibrous materials [53]. Taken together, this opens up new opportunities to test the effect of tailored fibrous fillers.

The reproducibility and usefulness of the entire technique based on the effect of intentional filament stringing has been demonstrated which means that: (i) acoustic material with a designed pore network, can in principle be produced with (or without) fibres in the pores or slits; (ii) the amount, thickness and type of fibres can be controlled using 3D printing parameters, in particular those related to retraction, but can also be precisely designed using *FullControl GCODE Designer*; (iii) sound absorption curves measured for acoustic material samples, manufactured using the same 3D printer, filament material, printing parameters and extrusion paths, are essentially identical, and (iv) fibres intentionally produced in slits or pores by filament stringing significantly increase sound absorption. We have proposed effective modelling technique that takes into account the presence of fibres inside slits (or pores, cavities, etc.). In this approach, the air inside the slits containing the fibres is replaced by an equivalent-fluid model suitable for air-saturated fibrous materials. The intentional filament stringing is controllable and reproducible, and its effect is captured by the proposed acoustic model. Therefore, this approach can be used to prototype more efficient acoustic composites with complex pore networks filled with fibrous materials.

CRedit authorship contribution statement

Tomasz G. Zielinski: Writing – review & editing, Writing – original draft, Visualization, Software, Resources, Methodology, Investigation, Formal analysis, Conceptualization. **Marco D'Agostini:** Writing – review & editing, Visualization, Software, Resources. **Andrew Gleadall:** Writing – review & editing, Visualization, Software. **Rodolfo Venegas:** Writing – review & editing, Validation, Conceptualization. **Paolo Colombo:** Writing – review & editing, Supervision. **Giorgia Franchin:** Writing – review & editing, Conceptualization.

Declaration of competing interest

The authors declare that they have no known competing financial interests or personal relationships that could have appeared to influence the work reported in this paper.

Acknowledgements

This research was financially supported by the National Science Centre (NCN), Poland, under Grant Agreement No. 2021/41/B/ST8/04492. R. Venegas acknowledges support from the Chilean National Agency for Research and Development (ANID) through ANID FONDECYT Grant No. 1211310.

This work is dedicated to Professor Keith Attenborough to celebrate 50 years of his research in acoustics.

Appendix A. Numerical calculations: Poisson problem for thermal diffusion

The concept of thermal permeability and thermal tortuosity was introduced by Lafarge in 1993 and 1997 [46]. To determine these macro-parameters, a dedicated Poisson problem for thermal diffusion in the fluid-saturated pores has to be solved [46,36,37]. Generally, the problem is defined in the fluid domain of a periodic elementary volume that is representative for a porous material. In the present study, the pore network is fully represented by the two-dimensional slit pattern inside the circular surface element A which is the cross-section of a cylindrical sample (or impedance tube with the surface area $A = \pi R^2$). Fig. A.1 (a,b)

shows an example of such a cross-section: the top surface of a “straight” sample 3D printed from purple ABS. The fluid domain inside this circular element is A_F (its surface area is $A_F = \phi A$ where ϕ is the porosity). The Poisson problem for thermal diffusion in a porous material saturated with fluid is defined as follows

$$\begin{aligned} -\nabla^2 \theta &= 1 & \text{in } A_F, \\ \theta &= 0 & \text{on } \partial A_F, \end{aligned} \quad (\text{A.1})$$

where the unknown variable θ can be treated as a field of temperature (or rather an excess from the ambient temperature) normalised to the unit of permeability (m^2). The boundary ∂A_F is formed from the solid walls surrounding the fluid domain A_F , and the homogenous Dirichlet boundary condition simulates the isothermal state on solid walls (the solid skeleton can be treated as a thermostat maintaining the ambient temperature, because the heat capacity and thermal conductivity of a solid are much greater than those of a fluid). The static thermal permeability Θ_0 is computed as an average of the field θ over the entire representative element of porous medium, i.e., in this study, over the entire cross-section A , namely

$$\Theta_0 = \langle \theta \rangle_A = \frac{1}{A} \int_A \theta \, dA = \phi \Psi_0, \quad \Psi_0 = \langle \theta \rangle_{A_F} = \frac{1}{A_F} \int_{A_F} \theta \, dA. \quad (\text{A.2})$$

Here, $\langle \dots \rangle_A$ is the averaging operator over the entire representative element, i.e. cross-section A , while $\langle \dots \rangle_{A_F}$ is the averaging operator over the fluid domain A_F within this element. Note that $\langle \dots \rangle_A = \phi \langle \dots \rangle_{A_F}$. Therefore, Ψ_0 is an average of θ over the fluid domain. The static thermal tortuosity is calculated as

$$\alpha_{0t} = \phi \frac{\langle \theta^2 \rangle_A}{\langle \theta \rangle_A^2} = \frac{\langle \theta^2 \rangle_{A_F}}{\langle \theta \rangle_{A_F}^2}. \quad (\text{A.3})$$

Numerical calculations aimed at solving the problem described above were carried out for all “straight” samples 3D printed for this study. Here, we demonstrate this procedure using the “straight” purple sample as an example. The surface scan of this sample, shown in Fig. A.1 (a), was used to generate a finite element mesh on the fluid domain, see Fig. A.1 (b). The two-dimensional mesh was used to calculate the porosity and characteristic length, and to perform the finite element analysis of the Poisson problem. The result of this analysis, i.e. the θ variable field shown in Fig. A.1 (c), was used to calculate Ψ_0 and Θ_0 , see Equation (A.2). Eventually, this single numerical simulation served to determine all the necessary macro-parameters and effective properties for materials with straight and twisted slit patterns, using analytical formulas derived in Section 3.

Appendix B. Tortuosity of twisted slits and helical channels

Consider a helical channel with radius R_n and pitch H_n , having a constant circular cross section of radius much smaller than R_n , see Fig. B.1 (a). The kinematic tortuosity of such a channel is equal to its geometric tortuosity, namely

$$\alpha_n = (L_n/H_n)^2, \quad (\text{B.1})$$

where

$$L_n = \sqrt{H_n^2 + (2\pi R_n)^2} = H_n \sqrt{1 + (2\pi R_n/H_n)^2} \quad (\text{B.2})$$

is the length of one complete helix turn. Such a helical channel is created by twisting a straight cylindrical channel (with the same circular cross section) around an axis parallel to its axis and located at a distance R_n . Let us define a twist angle Ω with respect to the height H of the cylindrical channel (cylindrical sample), see Fig. B.1 (a), which means that for any radius R_n the helix pitch is the same and equals

$$H_n = H_h = \frac{2\pi}{\Omega} H. \quad (\text{B.3})$$

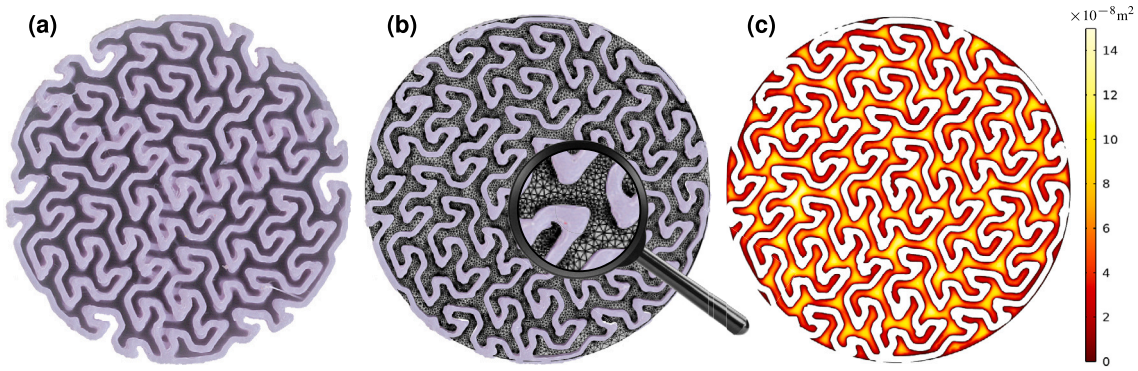


Fig. A.1. “Straight” purple ABS sample: (a) surface scan, (b) finite element mesh in the fluid domain, (c) finite element calculation results, i.e. the θ variable of the solved Poisson problem.

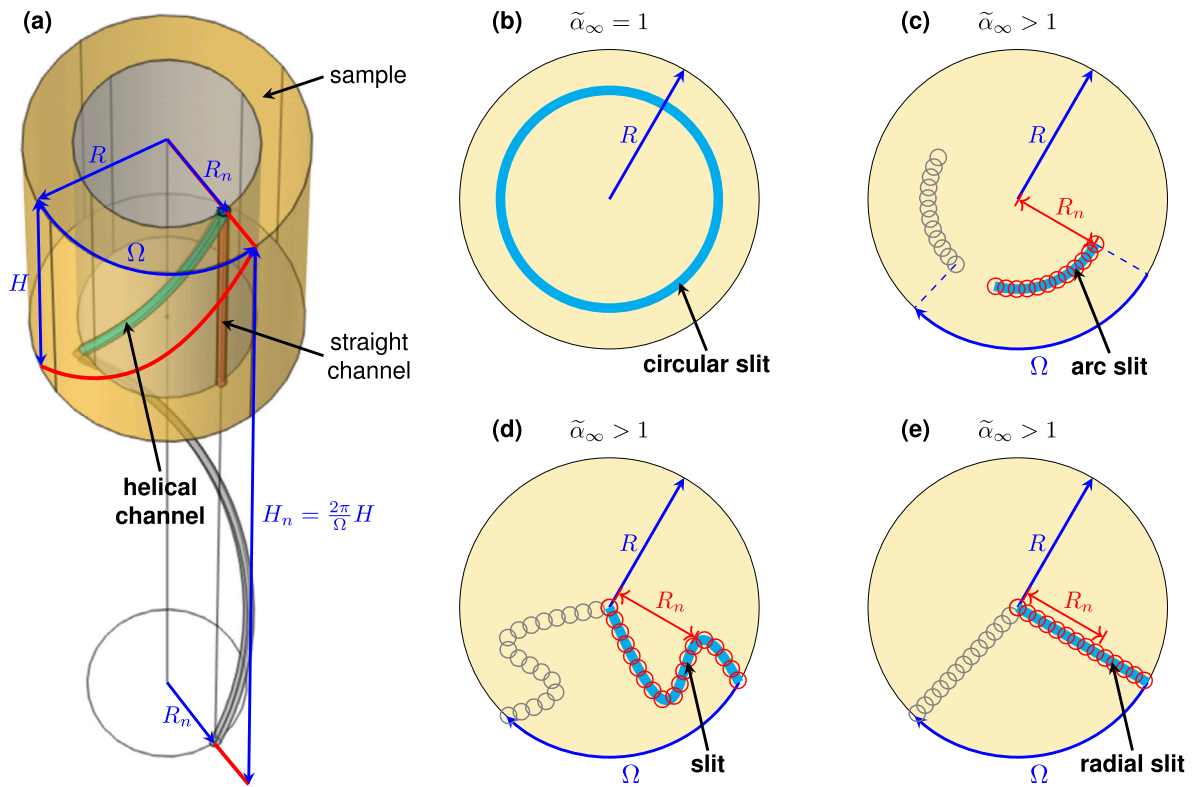


Fig. B.1. (a) A helical channel created from a straight cylindrical channel by twisting a cylindrical sample. (b,c,d,e) Top views of various slits in a cylindrical sample with small cylindrical channels (marked by red circles) arranged along the slits; when the sample is twisted, these channels change into helical channels (grey circles mark their entries at the bottom of the twisted sample).

Note that $H_h = H$, when the twist is a full rotation, i.e. for $\Omega = 2\pi$. Since H_h is defined by the formula (B.3) with known values of Ω and H , the tortuosity of each helical channel created by such a twist depends on its radius R_n , i.e. on the distance from the axis of rotation, namely

$$\alpha_n = (L_n/H_h)^2 = 1 + (2\pi R_n/H_h)^2 = 1 + a^2 \xi_n^2, \quad (\text{B.4})$$

where

$$\xi_n = \frac{R_n}{R}, \quad a = \frac{2\pi R}{H_h} = \frac{\Omega R}{H}. \quad (\text{B.5})$$

Now, consider an arbitrary narrow slit in a cylindrical material sample with radius R and height H . Top views of four examples of such slits are shown in Fig. B.1 (b,c,d,e). The slit tortuosity is 1 but changes due to sample twist, except for the circular slit. To discuss the change in tortuosity, the slit can be mentally replaced by a series of overlap-

ping identical cylindrical channels arranged along the slit, see red circles in Fig. B.1 (c,d,e). When the cylindrical sample is twisted by an angle of Ω , each cylindrical channel is transformed into a helical channel of radius R_n (equal to its distance from the centre of the sample) and tortuosity α_n defined by the formula (B.4). Except for the special case of the circular slit which remains unchanged after twisting, see Fig. B.1 (b), the tortuosity of the other slits increases and can be considered as a combination of the tortuosities of the helical channels that replace it, see Fig. B.1 (c,d,e).

Let the cylindrical sample (with radius R and height H) has one or more identical narrow slits, e.g., three identical PGC-based slits. The tortuosity $\tilde{\alpha}_\infty$ of such a slotted sample after being twisted by an angle of Ω is equal to the tortuosity of the twisted slit. There exists $R_h \leq \max(R_n) < R$ such that the tortuosity of a helical channel with radius R_h (formed by twisting the corresponding cylindrical channel by an angle

of Ω) is equal to $\tilde{\alpha}_\infty$. This is because the twisted slit tortuosity $\tilde{\alpha}_\infty$ cannot be greater than the highest of the tortuosities of the helices arranged along it.

The values of $\tilde{\alpha}_\infty$ and R_h depend on the slit pattern, but we can try to estimate them for continuous slits that run from the centre to the edge of the sample, see Fig. B.1 (d,e). First, recall that each helical channel has the same cross-sectional area A_h . The volume V_n and length L_n of the helical channel n are

$$V_n = A_h L_n = A_h H_h \sqrt{1 + a^2 \xi_n^2}, \quad L_n = H_h \sqrt{1 + a^2 \xi_n^2}. \quad (\text{B.6})$$

Suppose that for slits such as those shown in Fig. B.1 (d,e), the twisted slit tortuosity $\tilde{\alpha}_\infty$ can be approximated by a volumetric average of the tortuosities α_n of the helical channels arranged along it, namely

$$\tilde{\alpha}_\infty \approx \frac{\sum_n \alpha_n V_n}{\sum_n V_n} = \frac{\sum_n \alpha_n L_n}{\sum_n L_n} = \frac{\sum_n (1 + a^2 \xi_n^2) \sqrt{1 + a^2 \xi_n^2}}{\sum_n \sqrt{1 + a^2 \xi_n^2}}. \quad (\text{B.7})$$

Note that since A_h is the same for each channel n , the contribution of α_n to the value of $\tilde{\alpha}_\infty$ depends on the helix length, or rather on the ratio L_n/H_h . We can calculate $\tilde{\alpha}_\infty$ from a continuous distribution of helices along the radial slit shown in Fig. B.1 (e), using integration with respect to $\xi = \xi_n \in [0, 1]$ as follows

$$\tilde{\alpha}_\infty \approx \frac{\int_0^1 (1 + a^2 \xi^2) \sqrt{1 + a^2 \xi^2} d\xi}{\int_0^1 \sqrt{1 + a^2 \xi^2} d\xi} = \frac{(5a + 2a^3) \sqrt{1 + a^2} + 3 \operatorname{arcsinh} a}{4a \sqrt{1 + a^2} + 4 \operatorname{arcsinh} a}. \quad (\text{B.8})$$

Note that for $\Omega = 0$ (i.e. no twisting): $a = 0$ and $\lim_{a \rightarrow 0} \tilde{\alpha}_\infty = 1$. Using Equations (B.4) and (B.5), we can define the ratio

$$\xi_h = \frac{R_h}{R} = \frac{\sqrt{\tilde{\alpha}_\infty - 1}}{a}, \quad (\text{B.9})$$

assuming that $R_n = R_h$ is the radius of the helix with tortuosity $\alpha_n = \tilde{\alpha}_\infty$. For the data used in this study, i.e. $\Omega = 103^\circ$, $R = 14.5$ mm, and $H = 40.5$ mm, we obtain: $\tilde{\alpha}_\infty = 1.15$ and $\xi_h = 0.6$. These estimates proved to be valid for the PGC-based slits. Finally, recall that $\alpha_\infty = \tilde{\alpha}_\infty (1 + c_a)$, but the gain in tortuosity due to twisting by angle $\Omega = 103^\circ$ is predominant and amounts to 0.15.

Data availability

Data will be made available on request.

References

- [1] Wojciechowski B, Xue Y, Rabbani A, Bolton JS, Sharma B. Additively manufactured spinoid sound absorbers. *Addit Manuf* 2023;71:103608. <https://doi.org/10.1016/j.addma.2023.103608>.
- [2] Gui Y, Fei Z, Zhao S, Zhang Z, Shao H, Chen J, et al. High-strength and multifunctional honeycomb polyimide aerogel fabricated by a freeze casting-assisted extrusion printing and building block-assembly strategy for sound absorbing metamaterials. *Addit Manuf* 2023;77:103799. <https://doi.org/10.1016/j.addma.2023.103799>.
- [3] Li X, Chua JW, Yu X, Li Z, Zhao M, Wang Z, et al. 3D-printed lattice structures for sound absorption: current progress, mechanisms and models, structural-property relationships, and future outlook. *Adv Sci* 2024;11:2305232. <https://doi.org/10.1002/advs.202305232>.
- [4] Cavalieri T, Boulvert J, Romero-García V, Gabard G, Escoufflaire M, Regnard J, et al. Rapid additive manufacturing of optimized anisotropic metaporous surfaces for broadband absorption. *J Appl Phys* 2021;129(11):115102. <https://doi.org/10.1063/5.0042563>.
- [5] Boulvert J, Humbert T, Romero-García V, Gabard G, Fotsing ER, Ross A, et al. Perfect, broadband, and sub-wavelength absorption with asymmetric absorbers: realization for duct acoustics with 3D printed porous resonators. *J Sound Vib* 2022;523:116687. <https://doi.org/10.1016/j.jsv.2021.116687>.
- [6] Cai X, Guo Q, Hu G, Yang J. Ultrathin low frequency sound absorbing panels based on coplanar spiral tubes or coplanar Helmholtz resonators. *Appl Phys Lett* 2014;105:121901. <https://doi.org/10.1063/1.4895617>.
- [7] Prasetyo I, Anwar K, Brahmana F, Sakagami K. Development of stackable subwavelength sound absorber based on coiled-up system. *Appl Acoust* 2022;195:108842. <https://doi.org/10.1016/j.apacoust.2022.108842>.
- [8] Zielirski TG, Opiela KC, Dauchez N, Boutin T, Galland M-A, Attenborough K. Extremely tortuous sound absorbers with labyrinthine channels in non-porous and microporous solid skeletons. *Appl Acoust* 2024;217:109816. <https://doi.org/10.1016/j.apacoust.2023.109816>.
- [9] Gibson I, Rosen D, Stucker B. *Additive manufacturing technologies: 3D printing, rapid prototyping, and direct digital manufacturing*. 2nd edition. New York: Springer; 2015.
- [10] Kennedy J, Flanagan L, Dowling L, Bennett GJ, Rice H, Trimble D. The influence of additive manufacturing processes on the performance of a periodic acoustic metamaterial. *Int J Polym Sci* 2019;2019:7029143. <https://doi.org/10.1155/2019/7029143>.
- [11] Zielirski TG, Opiela KC, Pawłowski P, Dauchez N, Boutin T, Kennedy J, et al. Reproducibility of sound-absorbing periodic porous materials using additive manufacturing technologies: round robin study. *Addit Manuf* 2020;36:101564. <https://doi.org/10.1016/j.addma.2020.101564>.
- [12] Ciochon A, Kennedy J, Leiba R, Flanagan L, Culleton M. The impact of surface roughness on an additively manufactured acoustic material: an experimental and numerical investigation. *J Sound Vib* 2023;546:117434. <https://doi.org/10.1016/j.jsv.2022.117434>.
- [13] Matei S, Pop MA, Zaharia S-M, Coşniţă M, Croitoru C, Spîrchez C, et al. Investigation into the acoustic properties of polylactic acid sound-absorbing panels manufactured by 3D printing technology: the influence of nozzle diameters and internal configurations. *Materials* 2024;17:580. <https://doi.org/10.3390/ma17030580>.
- [14] Zielirski TG, Dauchez N, Boutin T, Leturia M, Wilkinson A, Chevillotte F, et al. Taking advantage of a 3D printing imperfection in the development of sound-absorbing materials. *Appl Acoust* 2022;197:108941. <https://doi.org/10.1016/j.apacoust.2022.108941>.
- [15] Ciochon A, Kennedy J. Efficient modelling of surface roughness effects in additively manufactured materials. *Appl Acoust* 2024;220:109953. <https://doi.org/10.1016/j.apacoust.2024.109953>.
- [16] Olny X, Boutin C. Acoustic wave propagation in double porosity media. *J Acoust Soc Am* 2003;114:73–89. <https://doi.org/10.1121/1.1534607>.
- [17] Venegas R, Boutin C. Enhancing sound attenuation in permeable heterogeneous materials via diffusion processes. *Acta Acust Acust* 2018;104:623–35. <https://doi.org/10.3813/AAA.919202>.
- [18] Venegas R, Zielirski TG, Núñez G, Bécot F-X. Acoustics of porous composites. *Composites, Part B, Eng* 2021;220:109006. <https://doi.org/10.1016/j.compositesb.2021.109006>.
- [19] Carbajo J, Molina-Jordá JM, Maiorano LP, Fang NX. Sound absorption of macro-perforated additively manufactured media. *Appl Acoust* 2021;182:108204. <https://doi.org/10.1016/j.apacoust.2021.108204>.
- [20] Kara Y, Kovács NK, Nagy-György P, Boros R, Molnár K. A novel method and print-head for 3D printing combined nano-/microfiber solid structures. *Addit Manuf* 2023;61:103315. <https://doi.org/10.1016/j.addma.2022.103315>.
- [21] Reizabal A, Kangur T, Saiz PG, Menke S, Moser C, Brugger J, et al. MEWron: an open-source melt electrowriting platform. *Addit Manuf* 2023;71:103604. <https://doi.org/10.1016/j.addma.2023.103604>.
- [22] Johnston W, Sharma B. Additive manufacturing of fibrous sound absorbers. *Addit Manuf* 2021;41:101984. <https://doi.org/10.1016/j.addma.2021.101984>.
- [23] Halbrecht A, Kinsbursky M, Poranne R, Serman Y. 3D printed spacer fabrics. *Addit Manuf* 2023;65:103436. <https://doi.org/10.1016/j.addma.2023.103436>.
- [24] Johnston W, Godakawala J, Gatti C, Keshavanarayana S, Sharma B. Fibro-porous materials: 3D-printed hybrid porous materials for multifunctional applications. *Addit Manuf* 2024;94:104470. <https://doi.org/10.1016/j.addma.2024.104470>.
- [25] Lomte A, Xue Y, Johnston W, Song G, Bolton JS, Sharma B. Acoustic modeling of three-dimensional-printed fibrous sound absorbers. *J Acoust Soc Am* 2024;156(6):3757–71. <https://doi.org/10.1121/10.0034429>.
- [26] Gleadall A. FullControl GCode designer: open-source software for unconstrained design in additive manufacturing. *Addit Manuf* 2021;46:102109. <https://doi.org/10.1016/j.addma.2021.102109>.
- [27] Cano-Vicent A, Tambuwala MM, Hassan SS, Barh D, Aljabali AA, Birkett M, et al. Fused deposition modelling: current status, methodology, applications and future prospects. *Addit Manuf* 2021;47:102378. <https://doi.org/10.1016/j.addma.2021.102378>.
- [28] Weisstein EW. MathWorld – A Wolfram Web Resource: Peano-Gosper curve (last viewed on April 15, 2025). Available from: <https://mathworld.wolfram.com/Peano-GosperCurve.html>, 2025.
- [29] Mandelbrot BB. *Fractals: form, chance, and dimension*. Revised edition. New York, NY, USA: W. H. Freeman and Company; 1977.
- [30] Ustyantsev A. gCodeViewer: GCode analyzer/visualizer (last viewed on April 15, 2025). Available from: <https://gcode.ws/>.
- [31] Alafaghani A, Qattawi A, Ablat MA. Design consideration for additive manufacturing: fused deposition modelling. *Open J Appl Sci* 2017;7:291–318. <https://doi.org/10.4236/ojapps.2017.76024>.
- [32] Wu P, Qian C, Okwudire CE. Modeling and feedforward control of filament advancement and retraction in material extrusion additive manufacturing. *Addit Manuf* 2023;78:103850. <https://doi.org/10.1016/j.addma.2023.103850>.

- [33] Gleadall A, Leas D. FullControl 0.1.1 [electronic resource: Python source code] (last viewed on April 15, 2025). Available from: <https://github.com/FullControlXYZ/fullcontrol>.
- [34] Sanchez-Palencia E. Non-homogenous media and vibration theory. Lecture notes in physics. Springer-Verlag; 1980.
- [35] Auriault J-L, Boutin C, Geindreau C. Homogenization of coupled phenomena in heterogeneous media. ISTE Ltd., John Wiley & Sons, Inc.; 2009.
- [36] Perrot C, Chevillotte F, Panneton R. Bottom-up approach for microstructure optimization of sound absorbing materials. *J Acoust Soc Am* 2008;124(2):940–8. <https://doi.org/10.1121/1.2945115>.
- [37] Zieliński TG, Venegas R, Perrot C, Červenka M, Chevillotte F, Attenborough K. Benchmarks for microstructure-based modelling of sound absorbing rigid-frame porous media. *J Sound Vib* 2020;483:115441. <https://doi.org/10.1016/j.jsv.2020.115441>.
- [38] Allard JF, Atalla N. Propagation of sound in porous media: modeling sound absorbing materials. 2nd ed. Chichester: John Wiley & Sons; 2009.
- [39] Ghanbarian B, Hunt AG, Ewing RP, Sahimi M. Tortuosity in porous media: a critical review. *Soil Sci Soc Am J* 2013;77(5):1461–77. <https://doi.org/10.2136/sssaj2012.0435>.
- [40] Holzer L, Marmet P, Fingerle M, Wiegmann A, Neumann M, Schmidt V. Tortuosity and microstructure effects in porous media. Cham: Springer International Publishing; 2023.
- [41] Attenborough K. Macro- and micro-structure designs for porous sound absorbers. *Appl Acoust* 2019;145:349–57. <https://doi.org/10.1016/j.apacoust.2018.10.018>.
- [42] Opiela KC, Zieliński TG, Attenborough K. Limitations on validating slitted sound absorber designs through budget additive manufacturing. *Mater Des* 2022;218:110703. <https://doi.org/10.1016/j.matdes.2022.110703>.
- [43] Attenborough K. Influence of periodically varying slit widths on sound absorption by a slit pore medium. *Materials* 2025;18(1):54. <https://doi.org/10.3390/ma18010054>.
- [44] Johnson DL, Koplik J, Dashen R. Theory of dynamic permeability and tortuosity in fluid-saturated porous media. *J Fluid Mech* 1987;176:379–402. <https://doi.org/10.1017/S0022112087000727>.
- [45] Champoux Y, Allard J-F. Dynamic tortuosity and bulk modulus in air-saturated porous media. *J Appl Phys* 1991;70:1975–9. <https://doi.org/10.1063/1.349482>.
- [46] Lafarge D, Lemarinier P, Allard JF, Tarnow V. Dynamic compressibility of air in porous structures at audible frequencies. *J Acoust Soc Am* 1997;102(4):1995–2006. <https://doi.org/10.1121/1.419690>.
- [47] Pride SR, Morgan FD, Gangi AF. Drag forces of porous-medium acoustics. *Phys Rev B* 1993;47(9):4964–78. <https://doi.org/10.1103/PhysRevB.47.4964>.
- [48] Attenborough K. Acoustical characteristics of rigid fibrous absorbents and granular materials. *J Acoust Soc Am* 1983;73:785–99. <https://doi.org/10.1121/1.389045>.
- [49] Petersen EE. Diffusion in a pore of varying cross section. *AIChE J* 1958;4(3):343–5. <https://doi.org/10.1002/aic.690040322>.
- [50] Umnova O, Tsiklauri D, Venegas R. Effect of boundary slip on the acoustical properties of microfibrous materials. *J Acoust Soc Am* 2009;126:1850–61. <https://doi.org/10.1121/1.3204087>.
- [51] ISO 10534-2. Determination of sound absorption coefficient and impedance in impedance tubes; 1998.
- [52] Opiela KC, Zieliński TG. Microstructural design, manufacturing and modelling of an adaptable porous composite sound absorber. *Composites, Part B, Eng* 2020;187:107833. <https://doi.org/10.1016/j.compositesb.2020.107833>.
- [53] Zieliński TG. Microstructure representations for sound absorbing fibrous media: 3D and 2D multiscale modelling and experiments. *J Sound Vib* 2017;409:112–30. <https://doi.org/10.1016/j.jsv.2017.07.047>.